

XMM-Newton and Swift observations of supergiant high mass X-ray binaries

C. Ferrigno¹, E. Bozzo^{1,2}, and P. Romano³

¹ Department of astronomy, University of Geneva, chemin d'Écogia, 16, CH-1290, Versoix, Switzerland
e-mail: carlo.ferrigno@unige.ch

² INAF-OAR, Via Frascati, 33, 00078 Monte Porzio Catone RM, Italy

³ INAF, Osservatorio Astronomico di Brera, Via E. Bianchi 46, I-23807, Merate, Italy

May 9, 2022

ABSTRACT

Wind-fed supergiant X-ray binaries are precious laboratories not only to study accretion under extreme gravity and magnetic field conditions, but also to probe still highly debated properties of massive star winds. These includes the so-called clumps, originated from the inherent instability of line driven winds, and larger structures. In this paper, we report on the results of the last (and not yet published) monitoring campaigns that our group has been carrying out since 2007 with both *XMM-Newton* and the *Swift* Neil Gehrels observatory. Data collected with the EPIC cameras on-board *XMM-Newton* allow us to carry out a detailed hardness ratio-resolved spectral analysis that can be used as an efficient way to detect spectral variations associated to the presence of clumps. Long-term observations with the XRT on-board *Swift*, evenly sampling the X-ray emission of supergiant X-ray binaries over many different orbital cycles, are exploited to look for the presence of large scale structures in the medium surrounding the compact objects. These can be associated either to corotating interaction regions or to accretion/photoionization wakes, as well as tidal streams. The results reported in this paper represent the outcomes of the concluded observational campaigns we carried out on the supergiant X-ray binaries 4U 1907+09, IGR J16393–4643, IGR J19140+0951, and XTE J1855–026, as well as the supergiant fast X-ray transients IGR J17503–2636, IGR J18410–0535, and IGR J11215–5952. All results are discussed in the context of wind-fed supergiant X-ray binaries and shall ideally serve to optimally shape the next observational campaigns aimed at sources in the same classes. We show in one of the paper appendices that IGR J17315–3221, preliminary classified in the literature as a possible supergiant X-ray binary discovered by *INTEGRAL*, is the product of a data analysis artifact and should thus be disregarded for future studies.

Key words. X-rays: binaries – X-rays: individual: 4U 1907+097 – X-rays: individual: IGR J19140+0951 – X-rays: individual: IGR J17503–2636 – X-rays: individual: IGR J17315+3221 – X-rays: individual: IGR J16393–4643 – X-rays: individual: IGR J18410–0535 – X-rays: individual: IGR J11215–5952 – X-rays: individual: XTE J1855–026 – stars: neutron

1. Introduction

Supergiant X-ray binaries (SgXBs) are a sub-class of high mass X-ray binaries (HMXBs) hosting most commonly a neutron star (NS) accreting from the wind of an OB supergiant. Apart from a few exceptions, the bulk of known systems in this class the compact object accretes from the in-flowing material that the massive companion loses through a fast and dense wind. The interest for SgXBs has been revived in the past years due to the recognition that these are key laboratories to investigate properties of the still highly debated massive star winds using the NS as a probe, especially in the domain of macro-clumping and large scale structures (see, e.g., Martínez-Núñez et al. 2017; Bozzo et al. 2016, and discussions therein).

In the framework of this renewed interest, our group has started a number of monitoring program of several SgXBs with both *XMM-Newton* and *Swift* to look for spectral variability in the X-ray emission of these sources that could be ascribed to the presence of massive structures in the stellar winds approaching the compact object and causing episodes of enhanced X-ray emission and/or obscuration of the high energy source (either the so-called “clumps” or even larger structures; see, e.g., Puls et al. 2008, and later in this section). Our monitoring program covers both sources within the sub-class of the “classical” SgXBs, showing a moderate X-ray variability, up to a factor of $\sim 10^3$ be-

tween quiescent and more active periods, and the supergiant fast X-ray transients (SFXTs), showing a much more pronounced X-ray variability up to a factor of 10^6 between quiescence and the brightest outbursts (see, e.g., Walter et al. 2015; Romano et al. 2015, and references therein).

As discussed by Bozzo et al. (2017a), hunting for spectral variations during SgXBs flares and outbursts to study the smaller stellar wind clumps requires sufficiently long and uninterrupted observations of these sources with X-ray instruments endowed with a large effective area in the soft X-ray domain (~ 3 keV). This is because the time intervals for the spectral extraction have a typical duration of few hundreds to thousands of seconds and enough X-ray counts need to be collected to perform meaningful spectral fits and disentangle both continuum and absorption column density variations. These integration times are set by the usual duration of flares and outbursts, which is limited to a few hours at the most, and the need of having as many probed as possible time intervals along the event rise and decay to study the dynamics of the accretion process (see, e.g., Bozzo et al. 2011, 2013b). So far, the EPIC cameras on-board *XMM-Newton* (Jansen et al. 2001) have proven to be the most effective instruments to pursue this goal (Bozzo et al. 2017a). The techniques we deployed to look for the spectral variability in the *XMM-Newton* data of classical SgXBs and SFXTs com-

Table 1: Properties of the sources studied in this paper.

ID	Companion	Distance kpc	Orbital period (d)	Spin period (s)	Super-orbital period (d)	$T_{\pi/2}$ (MJD)	e	ω (deg)	$a \sin i/c$ (lt-s)	B_{NS} 10^{12} G	Type
IGR J11215–5952	B0.5Ia	$6.5^{+1.1}_{-1.5}$	164.6 ± 0.1	186.78 ± 0.3	—	57925.5 ± 0.5	—	—	—	—	SFXT
IGR J16393–4643	OB ^a	12^a	4.2380 ± 0.0005	904.0 ± 0.1	14.9805 ± 0.0022^a	53418.3 ± 0.1	—	—	—	2.5 ± 0.1	Class.
IGR J17503–2636	OB ^a	10^a	—	—	—	—	—	—	—	2.0^a	SFXT
IGR J18410–0535	B1 Ib	3.2^a	—	—	—	—	—	—	—	—	SFXT
XTE J1855–026	BN0.2 Ia	10^a	6.0724 ± 0.0009	361.1 ± 0.4	—	51495.25 ± 0.002	0.04 ± 0.02	226 ± 15	80.5 ± 1.4	—	Class.
4U 1907+097	O8/O9 Ia	5^a	$8.3753^{+0.0003}_{-0.0002}$	$440.341^{0.012}_{-0.0017}$	—	$50134.76^{+0.16}_{-0.20}$	$0.28^{+0.10}_{-0.14}$	330 ± 20	83 ± 4	2.1	Class.
IGR J19140+0951	B0.5Ia/d	$2-5^a$	13.5527 ± 0.0001	5937 ± 219^a	—	52061.42^b	—	—	—	—	Class.

Notes. We indicated with orbital epoch ($T_{\pi/2}$) either the mid-eclipse time or the reference orbital epoch used for the ephemerides if the source is not eclipsing. In the case of IGR J11215–5952, we indicated as $T_{\pi/2}$ the mid-time of the 2017 outburst as reported by Sidoli et al. (2017, but see also Romano et al. 2009). In the case of IGR J16393–4641, $T_{\pi/2}$ corresponds to the epoch for which the minimum of the source lightcurve folded at the best known orbital period is at phase zero. For IGR J19140+0951, the reported orbital period is the one derived in Appendix A. We also reported, for the source for which it was possible, the orbit eccentricity e , the longitude of periastron ω , the projected semi-major axis length $a \sin i/c$, and the estimated NS magnetic field strength (B_{NS} , if derived from a confirmed CRSF). References are given in the text. ^(a) Tentative to be confirmed. ^(b) This is the apparent time of the minimum of the orbital profile in the *Swift*/BAT band, chosen conventionally.

prise an adaptively rebinned hardness ratio (HR) of the source energy-resolved lightcurves and a Bayesian block automatized selection of the time intervals corresponding to the most significant changes in the HR for the spectral extraction. These techniques are exhaustively described in a number of previous papers of ours, where we also illustrate the results obtained from several classical SgXBs and SFXTs (see, e.g., Bozzo et al. 2010, 2011, 2013b, 2015, 2017a; Ferrigno et al. 2020, and references therein). The HR-resolved spectral analysis that we have carried out so far revealed that during sufficiently bright flares and outbursts from the SgXBs we recorded an increase of the absorption column density preceding the brightening event and a decrease of the absorption close to the peak of the event. In several cases, we also observed a new increase of the absorption column density toward the end of the flare/outburst, as well as a change in the centroid energy of the iron line feature that is produced due to the fluorescence of the accretion X-rays onto the surrounding stellar wind material. In a few observations, episodes of enhanced absorption of the X-rays from the NS have been observed for as long as few hundreds of seconds also without being in coincidence with either a flare or an outburst. The physical picture that emerged from these results is that accretion in all analyzed SgXBs is compatible with occurring from a clumpy wind, where dense structures approach the compact object before being accreted and cause the local absorption column density to rise before the flare/outburst. The decrease of the absorption column density toward the peak of the event is ascribed to the photoionization effect of the enhanced X-rays onto the clump material, while the recombination following the beginning of the X-ray flux decay after the peak of the flare/outburst can explain the subsequent re-increase of the local absorption column density back to pre-rebrightening values. This scenario is more quantitatively confirmed for those cases where also a change in the centroid energy of the iron line is measured, as this provides a clearer identification of the ionization status of the stellar wind around the compact object (see, e.g., Bozzo et al. 2011, and references therein). Those episodes in which only a transient absorption of X-rays is visible without being associated with a rebrightening event are commonly ascribed to clumps passing in front of the compact object along the line of sight of the observer without intercepting its orbit and being (at least) partly accreted.

The results obtained from several observations of classical SgXBs and SFXTs suggest that the features measured through

the HR-resolved spectral analysis are relatively similar for both classes of objects. Although clumps are thus a key ingredient for the accretion in both sub-classes of sources, it seems necessary to assume that additional mechanisms are at work in SFXTs to explain their much more prominent X-ray variability. So far, considered mechanisms include gatings due to the NS rotation and magnetic field (Bozzo et al. 2008, 2017b) and the onset of a long-standing settling accretion regime (Shakura et al. 2012).

It should be mentioned that a number of flares, especially from the SFXTs, did not show evidence of substantial absorption column density enhancements (see, e.g., Bozzo et al. 2015). These events have been either interpreted as triggered by the above “additional mechanisms” without the (significant) intervention of clumps or as events observed through a direction such that our line of sight did not pass through (or intercept) the clump. As of today, the geometrical shape of the clumps (as well as other relevant parameters like the spatial extends in general, the masses and densities) are poorly constrained and thus geometrical effects have to be folded in the study of the accretion process as additional uncertainties.

Beside clumps, other massive structures are known to populate the accretion environments of NSs in SgXBs and can thus contribute to enhance the X-ray variability of these systems. Among such structures, there are the so-called “corotating interaction regions” (CIRs) which are extended structures originating from the surface of the supergiant star and extending up to several stellar radii. The CIRs are characterized by mild overdensity ratios compared to the rest of the stellar wind and since they do not perfectly co-rotate with the supergiant star, the interception of the NS with one of these structures could result in periodic enhancements of the X-ray luminosity and absorption column density at specific orbital phases (thus giving rise also to super-orbital modulations; see Bozzo et al. 2016, and references therein).

Similar enhancements at fixed orbital phases can also be produced by the presence of accretion and photoionization wakes, as well as tidal streams. Accretion wakes are dense structures partly surrounding the compact object and produced by the focusing of the stellar wind medium by the NS gravitational influence, while photoionization wakes are regions where the over-density (compared to the surrounding accretion medium) is due to the X-ray photoionization of the stellar wind and its partial stagnation. Finally, tidal streams are possible only in those systems where

the supergiant companion nearly fills its Roche lobe (see, e.g., Manousakis & Walter 2011; Grinberg et al. 2017; Kretschmar et al. 2019, and references therein).

The study of orbital-phase dependent structures requires long-term observations covering as many orbital periods as possible. The reason is that the eventual spectral variability recorded from the data on a single specific orbital phase is likely to be dominated by the effect of short-term variations of the accretion environment associated to clumps (thousands of seconds to hours). Averaging data at the same orbital phase but collected over many different orbits ensures that the short-term variability of the clumps is “washed away” and spectral changes can be most likely ascribed to the presence of large scale stable structures. For these reasons, relatively short snapshots with the narrow field instrument X-ray Telescope (XRT, Burrows et al. 2005) on-board the Neil Gehrels *Swift* Observatory (Swift, Gehrels et al. 2004) carried out over several months (considering that the typical orbital period of an SgXB is of few tens of days at the most) provide us the most effective strategy to collect the required data for the analysis of large scale wind structures in classical SgXBs and SFXTs.

In this paper, we report on several *XMM-Newton* observations of classical SgXBs and SFXTs that were either not published nor yet analyzed with our techniques (see above) to reveal spectral variations that can be associated to the presence of clumps. These results complement those reported previously in our papers on this topic. Furthermore, we report for the first time on the analysis of monitoring observational campaigns performed with *Swift* /XRT on several classical SgXBs in order to investigate possible spectral variability as a function of the orbital phase. Although some of these data were already reported elsewhere, we systematically apply a technique that can most effectively be used to reveal the presence of large scale structures around the compact objects in these systems. We discuss then our results in the framework of wind accretion in neutron star SgXBs.

The sources investigated in this paper are listed in Table 1. We note that only in the case of 4U 1907+09 both kinds of observations to study the short and long-term spectral variability associated to clumps and larger wind scale structures are available. In all other cases, either focused *XMM-Newton* observations or longer-term *Swift*/XRT data have been collected. For XTE J1855–026, XRT data have been exploited to search for the short-term spectral variability associated to clumps because the observations were performed during a few rare bright outbursts of the source. In the case of IGR J17503–2636, the data from the XRT observational campaign could not be folded on the source orbital period as this is still unknown.

In Sect. 2, we describe the general analysis methods for *Swift* and *XMM-Newton*. In Sect. 3 we briefly describe each sources in our sample with an overview of the data-sets available for each of them, we detail specific analysis methods, the results we obtained, and their discussion. In Sect. 4, we draw the conclusions of our work.

2. General data analysis methods

2.1. *Swift*

All *Swift* data were uniformly processed and analyzed using the standard software (FTOOLS¹ v6.29b), calibration (CALDB²

20210915), and methods. The *Swift*/XRT data were processed and filtered with the task XRTPipeline (v0.13.6).

For all sources with available XRT data, we first extracted the average spectrum in each XRT observation to measure the 0.3–10 keV flux. Then, we computed, for each observation, the HR value using the source count-rate in the 0.3–4 keV and 4–10 keV energy bands. If an orbital period was available (4U 1907+09, IGR J16393–4643, IGR J19140+0951), we calculated the orbital phase corresponding to each XRT observation and chose eight phase bins that would yield a comparable number of source counts (4U 1907+09: ~ 2700 counts; IGR J16393–4643: ~ 1300 counts; IGR J19140+0951: ~ 900 counts). Using the above energy bands, we calculated the hardness ratio for each phase bin and plotted the hardness ratio as a function of the orbital phase.

We note that the XRT observations are generally composed of up to three snapshots with typical exposures of 300–1000 s. Therefore, none of the XRT observations is suitable to look for the known pulsations of some of the target sources (see Sect. 3); however, computing the HR in each of them rather than in the single snapshots ensures us that the effect of the pulse period energy dependence on the HR is averaged out. This is further strengthened by the fact that several different observations are averaged together in order to compute the HR in the defined orbital phase bins.

In order to investigate more in depth possible spectral variability in different orbital phase bins, as suggested by the HR variations, we extracted different source spectra for each of these bins, grouped them so as to have at least one count per bin, and fit them by using a simple absorbed power-law model in

XSPEC version 12.12.0. For the absorption column density, we adopted the TBABS component with *wilm* abundances (Wilms et al. 2000) and *vern* cross sections (Verner et al. 1996).

2.2. *XMM-Newton*

All *XMM-Newton* observation data files (ODFs) were processed by using the *XMM-Newton* Science Analysis System (SAS 20.0.0), following standard procedures³. We filtered out background flaring time intervals due to cosmic protons by extracting the 10–12 keV EPIC-pn lightcurve binned at 100 s and identifying a count rate with less than 0.1% probability to belong to a Gaussian distribution. We retained, however, any time interval with a count rate below 0.6 counts per second.

The regions adopted for the extraction of all source and background scientific products (lightcurves and spectra) were chosen by checking where the instrument point spread function includes an optimal fraction of the photons specific to each source, or by picking the maximum allowed radius when the observation was carried out in small-window mode (details for each source are specified in the following sub-sections). We extracted the spectra and lightcurves of the three EPIC cameras together with the associated ancillary and response matrices, using standard procedures.

We grouped all EPIC spectra using the algorithms described in Kaastra & Bleeker (2016) and adopted as baseline model a power-law affected at the lower energies by photoelectric absorption. In addition to what used for *Swift*/XRT data, we generally add an absorber partly covering the source (pcfabs in XSPEC). To find the best-fit parameters, we minimized Cash statistics with background correction (Cstat in XSPEC), using a standard Levenberg-Marquardt algorithm based on the CURFIT routine from Bevington and then computed uncertainties using a

¹ https://heasarc.gsfc.nasa.gov/ftools/ftools_menu.html.

² https://heasarc.gsfc.nasa.gov/docs/heasarc/caldb/caldb_intro.html.

³ <http://www.cosmos.esa.int/web/xmm-newton/sas-threads>.

Monte Carlo Markov chain exploiting the Goodman-Weare algorithm. We used 60 walkers, a burning phase of 6000, and a chain length of 36 000. Uncertainties were found by computing the appropriate percentiles in the posterior distributions. As customary, we used a logarithmic prior for normalization and column density, and a linear prior for the slope and covering fraction.

For each source observed by *XMM-Newton*, we extracted the EPIC-pn, MOS1, and MOS2 light curves in two energy bands by computing the band limits as the median photon energy in the EPIC-pn camera to optimize the computation of the hardness ratio (HR). We summed together all EPIC lightcurves of each source to improve the statistical uncertainties and compute the adaptively rebinned hardness ratio (HR; see [Bozzo et al. 2013a](#), for a description of the adaptive rebinning method). A typical minimum signal to noise ratio (S/N) of 25 was achieved for the different sources in each of the time bins of the summed lightcurves. We determined periods in which the HR changes significantly by a Bayesian block analysis optimized to identify the most relevant HR variations with a negligible number of false positives (we used the fitness for point measurements and $\text{ncp_prior}=3.98$, see [Scargle et al. 2013](#), Sect 3.3). In each of the identified intervals, we extracted the corresponding spectra using appropriate extraction regions as for the averaged spectra and constructed also the corresponding ancillary and response matrices.

All uncertainties in the measured parameters from each source in the following sub-sections are indicated at 68 % confidence level, unless stated otherwise.

3. Description of targets, analysis results, and discussion

3.1. 4U 1907+09

4U 1907+09 is a classical supergiant X-ray binary discovered in the '70s by the *Uhuru* satellite ([Forman et al. 1978](#); [Giacconi et al. 1972](#)) and hosting a slowly rotating NS (the spin period is ~ 437 s; [Makishima et al. 1984](#)) orbiting a O8/O9 Ia supergiant ([van Kerkwijk et al. 1989](#); [Cox et al. 2005](#)). The system orbital period is measured at ~ 8.38 d ([Marshall & Ricketts 1980](#); [in 't Zand et al. 1998](#)). The NS in this system is known to undergo episodes of spin torque reversal ([Fritz et al. 2006](#); [Inam et al. 2009](#)), to display occasional quasi-periodic oscillations at a frequency of about 65 mHz ([in 't Zand et al. 1998](#); [Mukerjee et al. 2001a](#)), and to be endowed with a magnetic field strength of $\sim 2 \times 10^{12}$ G (the estimate is provided by the presence of a well known cyclotron scattering feature in the source X-ray spectrum with a centroid energy of ~ 19 keV; see, e.g., [Hemphill et al. 2013](#); [Varun et al. 2019](#), and references therein). As most highly magnetized NSs in HMXBs, the compact object in 4U 1907+09 features a complex pulse profile, which is both energy and luminosity dependent. This has been the central subjects of several literature works on the source (see, e.g., [Mukerjee et al. 2001a](#); [Rivers et al. 2010](#); [Şahiner et al. 2012a](#); [Fürst et al. 2012](#)). In the X-ray band, this source displays a dipping behavior which has been known for decades but is yet not clearly understood ([in 't Zand et al. 1997](#); [Doroshenko et al. 2012](#)).

3.1.1. Data analysis and results

Our yet unpublished monitoring campaign on 4U 1907+09 with *Swift* /XRT was performed with a pace of two observations per week, each 1 ks long, spanning from February to September 2015 (ObsID 33483). The full log of the XRT observations is

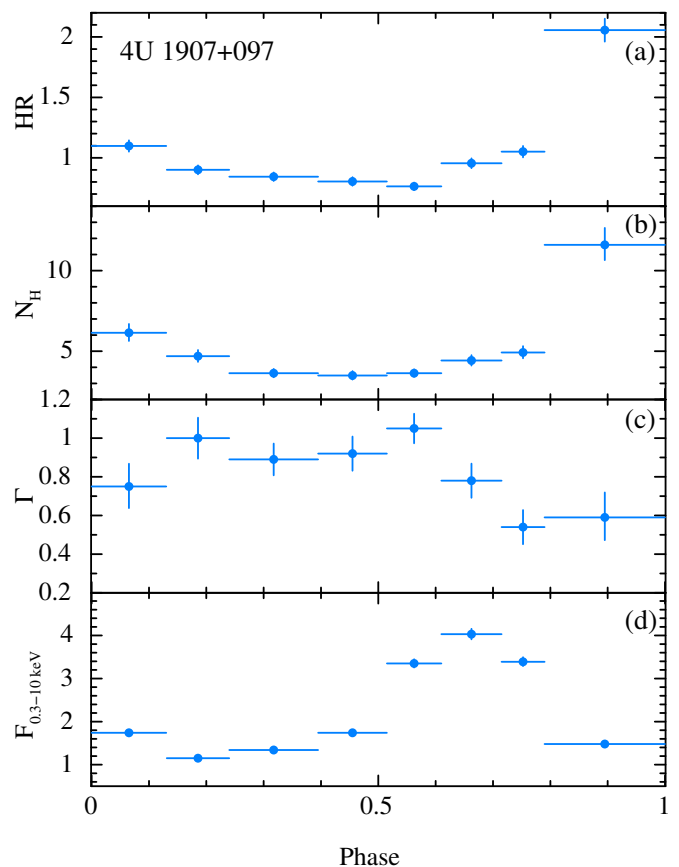


Fig. 1: *Swift*/XRT hardness ratio of 4U 1907+09, and best-fit parameters as a function of orbital phase (absorption column density N_H in units of 10^{22} cm^{-2} , power-law photon index Γ , and 0.3–10 keV flux not corrected for absorption in units of $10^{-10} \text{ erg cm}^{-2} \text{ s}^{-1}$).

provided in Table C.1. The results of fitting the average spectrum of the source in each XRT observation with an absorbed power law and the corresponding 0.3–10 keV flux are reported in Table C.1. We calculated the orbital phase corresponding to each XRT observation by using the source ephemerids published by [in 't Zand et al. \(1998\)](#), see Table 1) and grouped these observations in eight phase bins yielding a comparable number of source counts in each bin (~ 2700 counts). Fig. 1a shows the hardness ratio (4–10 keV / 0.3–4 keV) calculated for each of the eight time bins as a function of the orbital phase.

We also provide the first detailed analysis of an *XMM-Newton* observation that was previously reported by [Giménez-García et al. \(2015\)](#) extracting only the average spectrum for a study aimed primarily at the iron line emission. *XMM-Newton* observed 4U 1907+09 close to the epoch of periastron passage from 2009-04-18 at 12:16:25 to 2009-04-18 at 18:08:50 UT (OBSID 0555410101) for a total exposure time of about 20 ks. The EPIC-pn and MOS1 cameras were operated in timing mode, while the MOS2 in small window. The observation was not affected by any flaring background time interval and thus we retained the full observation exposure for the scientific analysis.

We extracted the EPIC-pn events in a region encompassing 80 % of the source net signal (from RAWX 27 to 45 included) and a background region with a width of 15 RAWX units (RAWX 7–22). We extracted the MOS1 source events in a circu-

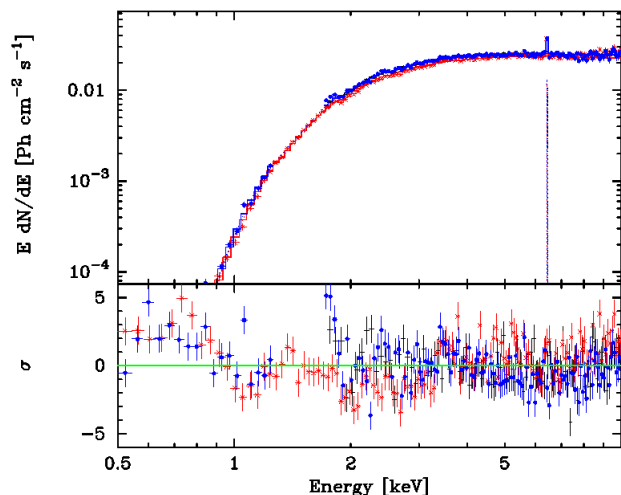


Fig. 2: 4U 1907+09 unfolded spectra obtained by using the entire exposure time available in the *XMM-Newton* OBSID. 0555410101 for the EPIC-pn (black points), MOS1 (red crosses), and MOS2 (blue circles) cameras. The residuals from the best fit model are reported in the bottom panel.

lar region with a radius of 800 pixels, centered at the source best position, while we chose a background region with a radius of 1200 pixels in an external CCD. We extracted the MOS2 source events encompassing 80% of the source net signal (RAWX 290–318 included) and a background box 2400×9600 pixels big located on an external CCD, unaffected by the source signal.

We found a satisfactory fit to the source averaged EPIC-pn, MOS1, and MOS2 spectra using an absorbed power-law model (we adopted the TBABS component as for *Swift*/XRT) and a partial covering (PCFABS in XSPEC). We also found a clear evidence of a prominent iron line at ~ 6.4 keV that was modeled in the fit using a Gaussian line with zero width. Due to the known calibration limitations for the different operating modes of the EPIC cameras, we restricted the fit to the energy range 1.1–10 keV for the EPIC-pn, 0.5–10 keV for the MOS1, and 0.5–1.1 keV plus 1.8–10 keV for the MOS2. Even though these choices exclude the obvious residuals linked to calibration uncertainties, scattered points remained visible especially below ~ 2 keV (see Fig. 2). We added a 2% systematic error on the spectrum to obtain a fit acceptable at the 4σ level, as the scattered residuals did not suggest the presence of an additional spectral component ($\chi^2 = 466$ for 352 degrees of freedom, hereafter d.o.f.)⁴. The best-fit parameters are reported in Table 2. Here and in the following, N_{H} is the absorption column density along the direction to the source (including the Galactic absorption), $N_{\text{H,pc}}$ is the column density of the partial absorber (representing the absorption column density local to the source), f is the covering fraction of the partial absorber, Γ is the power-law photon index, E_{Fe} and norm_{Fe} are the centroid energy and normalization of the Gaussian line representing the iron emission, and $F_{2-10 \text{ keV}}$ is the measured 2–10 keV power-law flux in units of $10^{-12} \text{ erg s}^{-1} \text{ cm}^{-2}$. Based on the current knowledge of the EPIC cameras calibrations, we consider the 7% difference in the MOS1 instrument normalization within the expected systematic calibration uncertainties of the different modes.

⁴ The χ^2 test statistics is appropriate here as in each spectral bin, there are at least 50 counts.

Table 2: Best-fit parameters obtained from the *XMM-Newton* data of 4U 1907+09 collected during the observation 0555410101.

Parameter	value	units
E_{Fe}	$6.412^{+0.009}_{-0.005}$	keV
norm_{Fe}	1.73 ± 0.10	$10^{-4} \text{ Ph s}^{-1} \text{ cm}^{-2}$
N_{H}	2.26 ± 0.11	cm^{-2}
$N_{\text{H,p.c.}}$	$3.23^{+0.20}_{-0.16}$	cm^{-2}
f	0.63 ± 0.04	
Γ	1.139 ± 0.009	
$F_{2-10 \text{ keV, EPIC-pn}}^a$	$351.5^{+1.1}_{-1.0}$	$10^{-12} \text{ erg s}^{-1} \text{ cm}^{-2}$
$F_{2-10 \text{ keV, MOS1}}$	325 ± 1	$10^{-12} \text{ erg s}^{-1} \text{ cm}^{-2}$
$F_{2-10 \text{ keV, MOS2}}$	352 ± 1	$10^{-12} \text{ erg s}^{-1} \text{ cm}^{-2}$
$\chi^2/\text{d.o.f.}$	466/353	

Notes. ^(a) Fluxes are not corrected for absorption.

From the cleaned EPIC-pn source event file list, we determined the best source spin period using the epoch-folding technique (see, e.g., D’Ai et al. 2011) at 2.2631(7) mHz and then extracted the background-subtracted energy-resolved lightcurves of the source in the 0.5–3 keV and 3–10 keV for all EPIC cameras binned at the above period, such that the variability eventually observed can be ascribed to the accretion environment and not the energy dependence of the source pulse period. The hardness ratio obtained after combining EPIC-pn, MOS1, and MOS2 data is shown in panel (a) of Fig. 3, while the corresponding count-rate is given in panel (b). The source displays a remarkable variability, with the largest changes in the HR visible toward the end of the observation, when the source enters a lower X-ray emission state.

We highlight as red vertical lines in panels (a) and (b) of Fig. 3 the time intervals with significant variations of the HR in which we extracted spectra to investigate the possible origin of this variability. We show the best-fit spectral parameters as function of time in Fig. 3. The centroid energy of the iron line is not shown because it remained stable at the value measured from the average spectrum to within the associated uncertainties. For each time interval, the EPIC-pn, MOS1, and MOS2 spectra were extracted and fit together with the same model used for the averaged spectrum (see earlier in this section). We note that fixing for all spectra the value of the TBABS absorption column did not result in acceptable fits, so we left this parameter free to vary also for the HR-resolved spectral analysis. It is evident from this figure that the time intervals during which the higher HR has been recorded are characterized by an overall enhanced local absorption column density ($N_{\text{H,pc}}$), while the covering fraction remains relatively stable around the average value and the powerlaw photon index displays only a modest softening compared to the initial part of the observation. Interestingly, the lowest values of the absorption column density are measured close to the peaks of the brightest emission episodes. We verified that the hardness is driven mainly by the variation of the column density in the partial-covering component by checking the linear correlation between HR and $N_{\text{H,pc}}$ that is significant at 99% confidence level using the r^2 statistics on a sample of 1000 bootstrapped data-sets, distributed according to the actual measurements. Other parameters are not significantly correlated to the HR. We investigated also the correlations between spectral parameters, but could not find any significant linear trend.

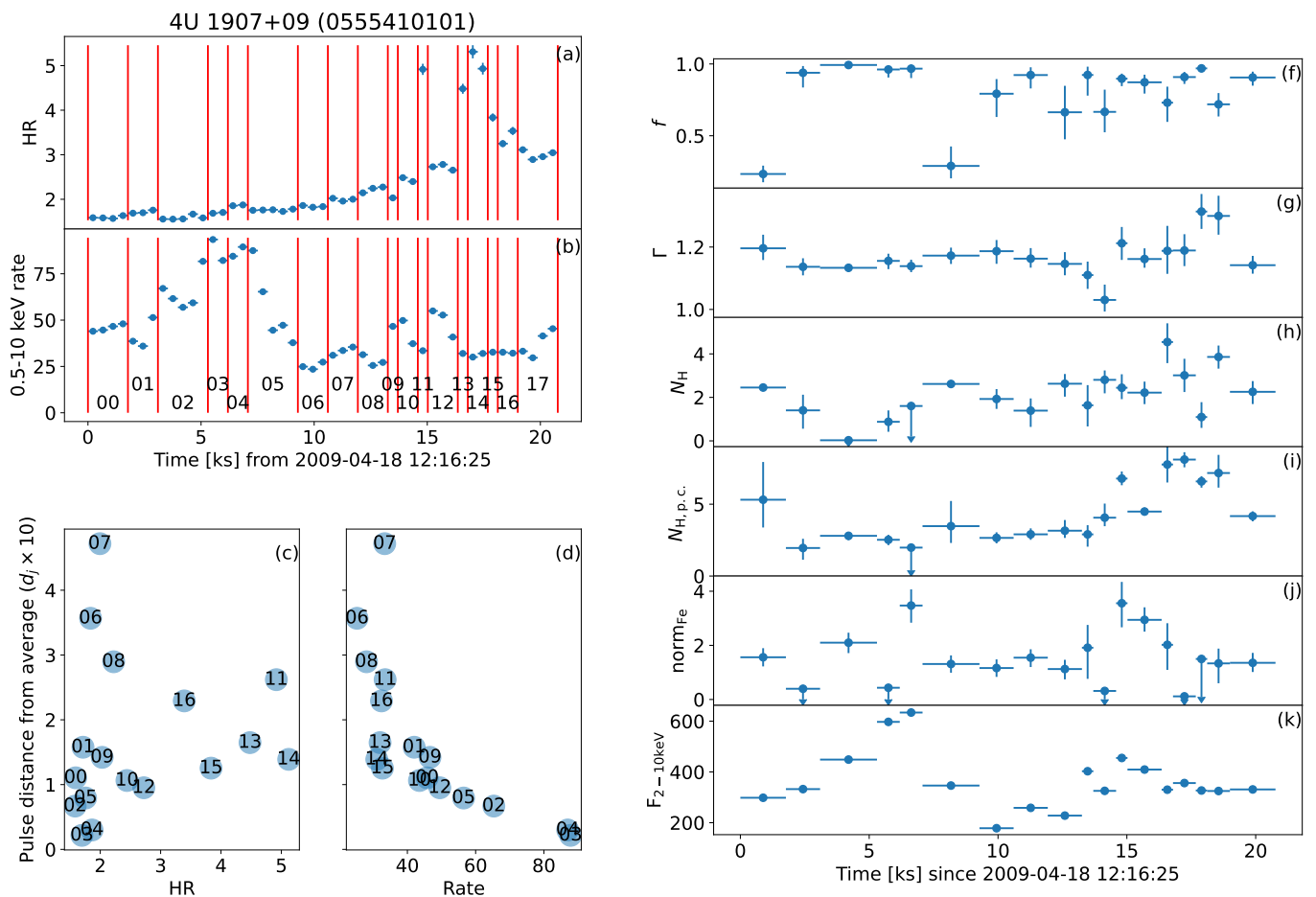


Fig. 3: *Top left, panel (a)*: hardness ratio of the combined EPIC-pn, MOS1, MOS2 light curves (3–10 keV/0.5–3 keV). *Top left, panel (b)*: total rate in the 0.5–10 keV energy range. *Bottom left, panel (c)*: distance d_j from the average for each pulse profile as function of HR. *Bottom left, panel (d)*: distance d_j from the average for each pulse profile as function of the total rate. The numbers indicate the different intervals identified in panel (b) (see eq. 1 for the definition of d_j). *Right*: plot of the best-fit parameters as a function of time obtained from the HR-resolved spectral analysis of the *XMM-Newton* observation of 4U 1907+09. The parameters reported in the different panels are those introduced in Table 2 and described in the text.

For each time interval of different hardness ratio in panels (a) and (b) of Fig. 3, we folded the total light curve at the NS spin period to extract the pulse profiles. In Fig. 4, we show the pulse profiles after dividing them for their average and displacing them vertically by ten times their distance from the average profile, computed as

$$d_j = \sum_{i=1}^{32} \frac{|p_{i,j} - \bar{p}_i|}{\sigma_{i,j}}, \quad (1)$$

where j represent the pulse-profile number, $p_{i,j}$ is the i -th bin of the j -th pulse profile, $\sigma_{i,j}$ the uncertainty, and \bar{p}_i is the average i -th bin of the average pulse profile. The label of each line represents the number of interval j from zero to 17, as indicated in panel (b) of Fig. 3. In this figure, we also show for each HR interval the pulse variability as function of the HR (panel c) and of the total rate (panel d).

The time intervals in which the source is brighter are characterized by pulse profiles that are more similar to the average profile. However, we note a pronounced variation in the shape

of the pulse profile, compared to the average shape, during the lower luminosity HR intervals. The most peculiarly shaped pulse profiles are recorded during the HR intervals 6–8, immediately following the brightest source emission phase toward the middle of the *XMM-Newton* observation. Intervals 13–15 are instead characterized by the highest HR values (and average fluxes) but the corresponding pulse profiles are relatively similar to the average one. Interval 11 has one of the highest recorded HR values, a relatively low flux, and is characterized by a shape of the pulse profile with intermediate properties between the average profile and those of the most peculiar intervals 6–8.

3.1.2. Discussion of the results

The *Swift*/XRT orbital monitoring of the source provided some interesting results. As shown in Fig. 1, the flux is remarkably peaked around phase 0.5–0.8, remaining virtually constant during the rest of the orbit. The source also displays a strongly variable absorption column density and photon index along the orbital phase. In particular, the evident spectral hardening around

Table 3: Results of the orbital phase-resolved spectral analysis conducted on the *Swift*/XRT observations of IGR J19140+0951.

Parameter	Orbital phase							
	0–0.205	0.205–0.270	0.270–0.375	0.375–0.500	0.500–0.625	0.625–0.750	0.750–0.835	0.835–1.000
n_{H}	$0.8^{+0.1}_{-0.1}$	$1.6^{+0.2}_{-0.2}$	$2.7^{+0.3}_{-0.3}$	$4.3^{+0.5}_{-0.4}$	$1.6^{+0.2}_{-0.2}$	$1.0^{+0.1}_{-0.1}$	$1.2^{+0.2}_{-0.1}$	$1.1^{+0.2}_{-0.1}$
Γ	$0.8^{+0.2}_{-0.2}$	$1.0^{+0.2}_{-0.2}$	$1.2^{+0.2}_{-0.2}$	$1.3^{+0.3}_{-0.3}$	$1.1^{+0.2}_{-0.2}$	$1.0^{+0.2}_{-0.2}$	$1.1^{+0.2}_{-0.2}$	$1.1^{+0.2}_{-0.2}$
$F_{0.3-10\text{keV}}$	$1.8^{+0.1}_{-0.1}$	$10.3^{+0.5}_{-0.4}$	$10.4^{+0.5}_{-0.5}$	$4.9^{+0.3}_{-0.2}$	$4.7^{+0.2}_{-0.2}$	$4.1^{+0.2}_{-0.2}$	$2.6^{+0.2}_{-0.1}$	$3.0^{+0.2}_{-0.2}$
Cstat/d.o.f.	479.7/488	440.6/521	423.5/511	387.6/464	417.3/520	383.4/478	352.7/445	405.2/457

Notes. We report the measured value of the absorption column density (N_{H} , in units of 10^{23} cm^{-2}), the power-law photon index (Γ), and the 0.3–10 keV flux (not corrected for absorption, in units of $10^{-11} \text{ erg cm}^{-2} \text{ s}^{-1}$).

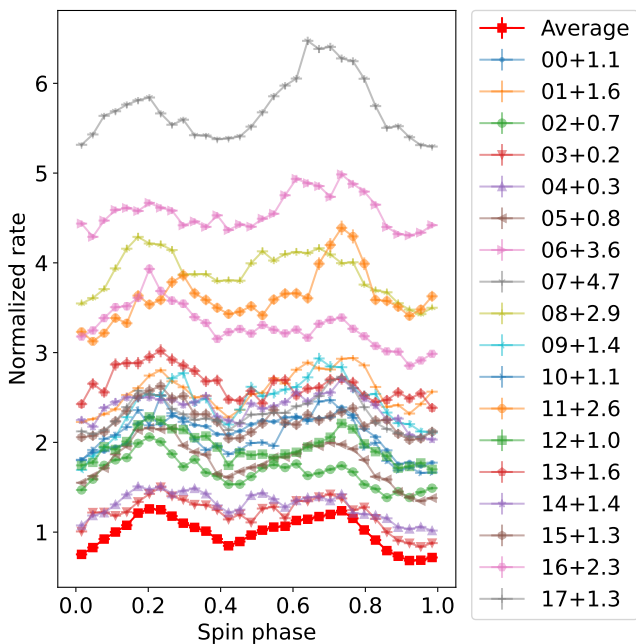


Fig. 4: Average and HR-resolved pulse profiles of 4U 1907+09 divided by their mean and vertically displaced by ten times their distance from the average, as computed in eq. (1). Labels represent the order of pulse profile as labelled in panel (a) of Fig. 3.

phase 0.8–1.0 is driven by both an increase by a factor of ~ 2 in the local absorption column density and a flattening of the spectral index. As the phase 0 in our calculation was assumed to be the same as that of in 't Zand et al. (1998), this point correspond to the epoch of the mean longitude 90° , that is when the NS is beyond the companion right along the line of sight to the observer. This occurs slightly after the periastron passage that corresponds to phase ~ 0.7 . Compatible results were obtained in the past by using *ASCA* and *RXTE* data (Roberts et al. 2001; Şahiner et al. 2012b), although the monitoring presented here with XRT provides an extension of the coverage at the softer X-rays (down to 0.3 keV) and the orbital phase-resolved spectral analysis is carried out by averaging multiple observations over several orbital cycles rather than making use of single short pointings (few ks) carried out at specific orbital phases within the same orbital revolution.

The flux increase close to periastron passage is to be expected in a moderately eccentric wind-fed SgXB, especially if the photoionization of the stellar wind by the accreting NS is rel-

atively low. This is due to the higher density of a line-driven wind closer to the supergiant star, as well as the decrease in the relative velocity between the NS and the companion's wind, both effects leading to an enhanced mass accretion rate onto the compact object (see, e.g., Bozzo et al. 2021, and references therein). The interpretation of the spectral hardening around phase 0.8–1.0 is less straightforward, and was largely debated also in the past (see Roberts et al. 2001, and references therein). The most widely accepted explanation is the presence of a trailing gas stream connecting the supergiant with the NS, similarly to what was considered to explain the case of the eccentric HMXB GX 301–2 (Leahy 1991; Leahy & Kostka 2008; Kostka & Leahy 2010). Although the statistics of the XRT data does not allow us to establish a firm conclusion, our findings are fully consistent with those reported in the past. Future observations carried out with grating instruments (as those on-board *XMM-Newton* and *Chandra*) might be exploited to further corroborate this scenario looking for changing photoionization lines as a function of the orbital phase as done previously in the case of the SgXB Vela X-1 (Watanabe et al. 2006).

The pointed *XMM-Newton* observation of 4U 1907+09 allowed us to study the variability of the source emission over short timescales, typical of the wind accretion process (see Sect. 1). Once the *XMM-Newton* lightcurve is binned at multiples of the best determined spin period, the observed variability can be ascribed to changes in the accretion environment surrounding the compact object and we noticed in Fig. 3 that the highest recorded values of the local absorption column density occur during periods where the source intensity is low. A similar behavior has been observed in other SgXBs and commonly ascribed to the presence of massive clumps passing occasionally in front of the NS along the line of sight to the observer without being accreted and thus without producing an enhanced X-ray emission. The HR-resolved spectral analysis reported in Fig. 3 supports this conclusion because it shows that $N_{\text{H,p.c.}}$ is the main driver of spectral variability during the second half of the observation. From the same figure, we also observe that there is a decrease of the local absorption column density around the peaks of the flares taking place during the first ~ 10 ks of the observation and that there are two sharp decreases on the covering fraction at the beginning of the observation (before the bright flares go off) and right after the end of the flaring period. Drops of the local absorption column density during the brightest emission periods are usually interpreted as due to the photoionization of the clumpy stellar wind by the X-rays from the compact object, while the initial low value of the covering fraction could indicate that there was a progressive fragmentation of a dense clump before the flaring period began. The recorded drop of the covering fraction after the flare could be explained in this context as the

residual (non-accreted) portion of the fragmented dense clump moving away from the compact object (see, e.g., [Bozzo et al. 2011](#), and discussions therein).

The average source pulse profile, mediated using the entire exposure time available of the *XMM-Newton* observation shows a spin-phase variability virtually identical to what has been reported previously (see, e.g., [in 't Zand et al. 1998](#)). A study of the variability of the pulse profile with the source intensity, at the best of our knowledge, was attempted in the past by [Roberts et al. \(2001\)](#) using four different *ASCA* observations (see also [Mukerjee et al. 2001b](#); [Fritz et al. 2006](#); [Rivers et al. 2010](#)). These data spanned a total range in the source X-ray luminosity of a factor of ~ 60 and highlighted some possible change in the pulse profile shape as a function of the intensity, but the statistics was rather low to perform any meaningful comparison among the different profiles. As shown in [Fig. 4](#) and [3](#), the relatively high statistics and uninterrupted exposure of the *XMM-Newton* observations allowed us to report here for the first time an analysis of the pulse profile resolved in intensity and HR. We found that the shape of the pulse profile displays a remarkable variability compared to the average profile, with the largest deviations being recorded during the intervals 6, 7, and 8 (see panel (d) of [Fig. 3](#)). These intervals correspond to a period of relatively faint emission from the source (combined count-rate from the EPIC cameras of $\lesssim 30$ cts s^{-1}) and immediately precedes the going off of two faint flares from the source during (and after) which the highest HR values are measured (see panels (a) and (b) of [Fig. 3](#)). As our HR-resolved spectral analysis demonstrated that the HR variations are driven by the increase of the local column density and since changes in the shape of the pulse profile in HMXBs are known to be associated to switching between different accretion geometries (see [Parmar et al. 1989](#), for an early discussion), we infer that the encounter of a stellar wind clump with a NS can sometimes alter the way in which the material is accreted and not only the mass accretion rate or the absorption. However, the two phenomena are not necessarily connected. Although this is a somewhat standard assumption in theoretical models proposed to interpret wind-fed systems (see, e.g., [Bozzo et al. 2008](#); [Shakura et al. 2012](#), and references therein), we are not aware of similar other evidence in SgXBs. This result could only be obtained by combining the HR-resolved spectral analysis with a HR-resolved study of the source pulse profile, a technique that our group plans now to exploit for additional bright sources within the SgXB class.

It is worth mentioning here that additional evidence in favor of the scenario proposed above could be obtained by performing a pulse-phase resolved spectral analysis of the source emission within each identified HR time interval in [Fig. 3](#) (panels (a) and (b)). Unfortunately, the statistics of the *XMM-Newton* data is not sufficient to carry out such analysis (only one single EPIC spectrum can be extracted for each HR time bin in order to achieve a meaningful spectral fit). This limitation cannot be overcome by using deeper observations with any currently available facility as the required statistics is limited by the X-ray photons collection capability of the existing instruments. This is directly related to the available effective area of the instrument, and under this respect the *XMM-Newton* EPIC cameras are already providing the best performances. Future instrumentation endowed with a much larger area in the soft X-ray domain, as the XIFU and WFI on-board *Athena* ([Barret et al. 2016](#); [Meidinger et al. 2015](#)) or the LAD on-board the *eXTP* ([Zhang et al. 2016](#)) or the *STROBE-X* ([Ray et al. 2019](#)) missions could provide the necessary advancements to unveil the nature of the pulse profile changes in 4U 1907+09 and other wind-fed systems.

3.2. IGR J19140+0951

IGR J19140+0951 was discovered by *INTEGRAL* in 2003 ([Hanikainen et al. 2004](#)) and later classified as a classical SgXB thanks to the identification of the optical counterpart as a B0.5 Ia star ([Torrejón et al. 2010](#)) and the detection of an orbital period of 13.5 d (see, e.g., [Wen et al. 2006](#), and references therein). The distance to the B0.5 Ia star has been recently determined using *Gaia* data from the originally estimated 3.6 kpc ([Torrejón et al. 2010](#)) to $2.8_{-2.3}^{+1.3}$ ([Arnason et al. 2021](#)). [Sidoli et al. \(2016\)](#) reported about the discovery of a possible pulsation period from a *Chandra* observation of the source at ~ 5937 s and a quasi-periodic oscillation (QPO) from an *XMM-Newton* observation of the source at a frequency of ~ 1.46 mHz. The QPO has been interpreted as due to the onset of a quasi-spherical accretion regime.

3.2.1. Data analysis and results

Our *Swift* /XRT monitoring campaign on IGR J19140+0951 was carried out in 2015 with a pace of two observations per week, each 1 ks long, spanning from February to September 2015 (ObsID 30393). These observations (see [Table C.2](#)), summing up to a total exposure of ~ 60 ks, cover a bit less than 17 revolutions of the system. The log of the XRT observations, [Table C.2](#), also shows for each XRT observation the orbital phase according to the ephemerides reported in [Table 1](#). We note that as the previous ephemerides of the source were published by [Corbet et al. \(2004\)](#) using *RXTE*/*ASM* data up to 2004 and since then additional 8 years of *ASM* data plus about 15 years of *Swift*/*BAT* monitoring data on the source have been made available, so we could refine the determination of the orbital period to the value reported in [Table 1](#) (all analysis details are provided in [Appendix A](#)). We also note that in the case of IGR J19140+0951 the spin period is not known and the tentatively reported one by [Sidoli et al. \(2016\)](#) is far too long to allow any meaningful search in the short XRT observations.

The plot of the source HR as a function of the orbital phase is shown in [Fig. 5a](#). We fit the eight spectra extracted from the 8 phase bins with an absorbed power-law and report the results in [Table 3](#) and [Fig. 5](#) (panels b–d).

For completeness, we mention here that the sole *XMM-Newton* observation of the source published by [Sidoli et al. \(2016\)](#) does not allow any HR-resolved spectral investigation, as the source was relatively faint during the time spanned by the *XMM-Newton* data and no flare was apparent from the source lightcurve (see [Fig. 3](#) in [Sidoli et al. 2016](#)).

3.2.2. Discussion of the results

The plot of the spectral parameters and HR as a function of the orbital phase ([Fig. 5](#)) obtained from the XRT monitoring of the source displays a rather intriguing variability with the peak of the X-ray flux measured at phase 0.2–0.4, which is consistent with the sharply peaked average orbital profile obtained in the 15–50 keV band using 15 years of continuous monitoring by *Swift*/*BAT* ([Fig. A.1](#)). We notice a steep increase in the absorption column density immediately following and reaching the maximum at phase 0.4–0.5. A similar increase of the source local absorption column density at specific orbital phases was already reported in the past by [Prat et al. \(2008\)](#). However, their measurements as a function of the orbital phase were affected by large uncertainties mainly due to the limited coverage below 3 keV. Our results show that the orbital variability of the flux and absorption column density in IGR J19140+0951 is much more

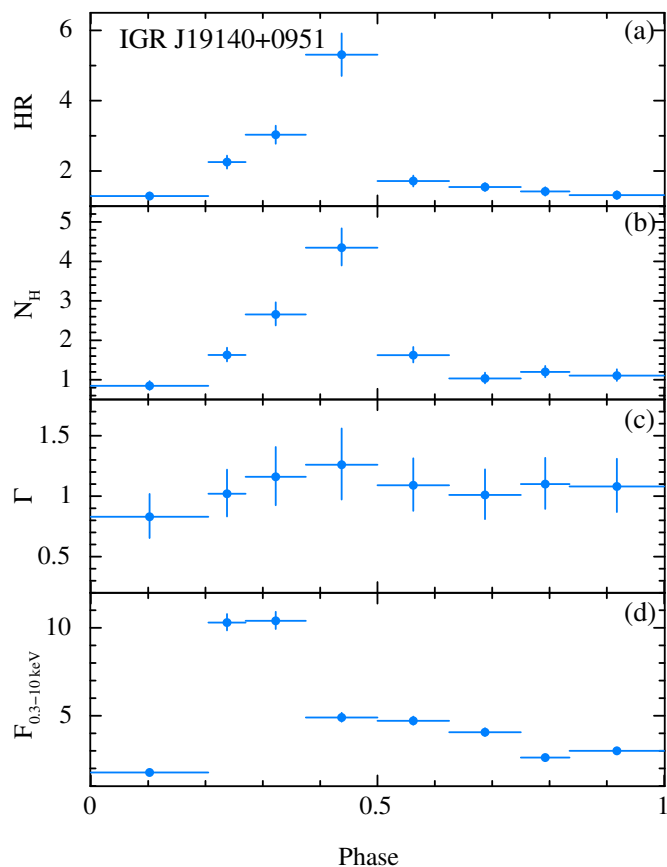


Fig. 5: Same as Fig. 1 but realized for IGR J19140+0951. Here the flux is given in units of 10^{-11} erg cm $^{-2}$ s $^{-1}$.

extreme than what was observed before and it is remarkably similar in what is observed from the much better studied source 4U 1907+09. In both systems, there is a shift in phase of about ~ 0.2 between the maximum of the flux and the maximum of the absorption column density, and the profile of the flux variability is also peaked at a restricted interval in the orbital phase (≤ 0.2). In both sources, there is also a relatively modest to no change in the power-law slope. We thus conclude that, most likely, the same scenario that has been proposed for 4U 1907+09 is also applicable to the case of IGR J19140+0951: this source shall be characterized by a non-negligible eccentricity and there should be a large structure located close to the NS and moving with the compact object, possibly a gas stream as indirectly proved in the case of 4U 1907+09. Although we cannot firmly exclude alternative scenarios, the data so far are compatible with this hypothesis and the similarity with the case of 4U 1907+09 provides support in the right direction.

A measurement of the eccentricity in the case of IGR J19140+0951 would be best obtained by following the evolution of the source spin period at different orbital phases. However, the possibly long spin period of the source (over 5 ks, to be confirmed, see Table 1) would make such measurements extremely time consuming for any sufficiently sensitive facility capable of performing uninterrupted observations of several tens of ks (e.g., the EPIC cameras on-board *XMM-Newton*). A validation of our proposed scenario for IGR J19140+0951 through the direct comparison with 4U 1907+09 could be obtained by exploiting also deep X-ray observations of the source at specific

orbital phases, especially around the peak of the absorption column density where emission/absorption lines can provide a measurement of the ionization status of the absorbing material and its position compared to both the NS and the supergiant companion.

3.3. IGR J11215–5952

IGR J11215–5952 is the only SFXT source displaying regular outburst at the periastron passage and having a well measured spin and orbital periods. The system hosts a ~ 187 s spinning NS orbiting every ~ 165 days around the B0.5 Ia companion, located at a distance of $6.5^{+1.1}_{-1.5}$ kpc (see Sidoli et al. 2020; Arnason et al. 2021, and references therein). The source has been observed many times with virtually all available X-ray facilities and the regularity of its luminosity variations allowed the scheduling of targeted X-ray observations right at the peak of the brightest emission periods. These observing campaigns were aimed at obtaining high S/N data and look for CRSFs, but so far no firm detection was reported (Sidoli et al. 2017, 2020). The role of clumps in the accretion process undergoing in this system is of wide interest because the supergiant star in IGR J11215–5952 showed evidence of a magnetized stellar wind and, when this magnetic field is carried by the clumps, it can lead to reconnections and subsequent bright episodes of X-ray emission. Such mechanism is one of the proposed scenarios to interpret the peculiar behavior of the SFXTs in X-rays (Hubrig et al. 2018).

3.3.1. Data analysis and results

We report on a new *XMM-Newton* observation of the source performed from 2021-01-25 at 23:32:04 to 2021-01-26 at 05:01:25 (OBSID 0862410301). Out of the 19.8 ks of EPIC-pn exposure, we retained 15.6 ks after removing periods of background flaring. For the EPIC-pn, we use a source extraction region with radius on 0.53 arcmin, based on the radius at which the surface brilliance of the source equals the surrounding background and an adjacent background region with radius of 1 arcmin. For MOS1, we use a source extraction region fixed to lie within the small windows of 0.47 arcmin and a background region with radius 1 arcmin in an external CCD. For MOS2, we used RAWX from 282 and 322 for the source, which encompasses 60% of the PSF, to avoid the contribution from a field source, and a background region with the shape of a box 8 \times 2 arcmin.

We extracted light curves in the 0.5–3.5 and 3.5–10 keV bands to compute the HR. We caught the source in an episode of decreasing flux characterized by a softening spectrum as evidenced in Fig. 6. We managed to describe both the average and HR-resolved spectra using a power-law modified by full neutral absorption (TBABS) and a partial covering component (PCFABS). The best C-stat is 238 as compared to 295 obtained using an absorbed power-law. To test the significance of the improvement, we simulated, for each best-fit model, 100 spectra with equivalent exposure and background using parameters extracted from the chain used to compute uncertainties. For each simulated spectrum, we performed a fit with the same model. For the absorbed power-law, 20% of the simulated spectra have higher C-stat than the real spectrum, while adding a partial covering component this fraction raises to 93%, indicating a significant improvement. As it can be appreciated in Fig. 6, the parameter showing the strongest variability is the power-law photon index, suggesting that the softening is mostly linked to intrinsic change in the emission rather than to intervening absorption. We investi-

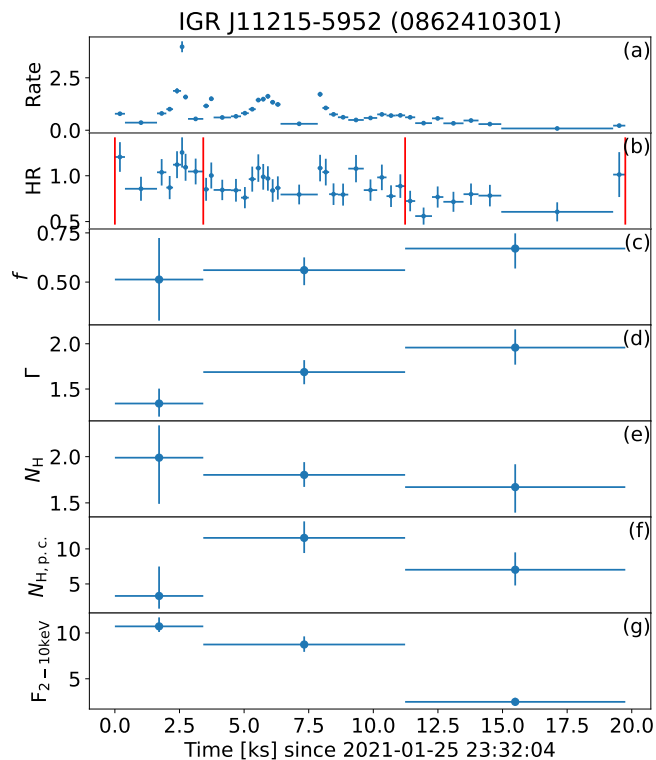


Fig. 6: Plot of light curve, HR, and best-fit parameters as a function of time obtained from the HR-resolved spectral analysis of the *XMM-Newton* observation of IGR J11215–5952. *Panel (a)*: the source count rate in the 0.5–10 keV bands, after adaptive rebinning with minimum S/N of 15 in the light curve extracted for 0.5–3 keV; *Panel (b)*: HR between the 3–10 keV and 0.5–3 keV energy-resolved lightcurves with the identified time intervals for the spectral extraction (marked with red lines); *Panel (c)*: f , the covering fraction of the partial absorber; *panel (d)*: Γ , the power-law photon index; *panel (e)*: N_{H} , the absorption column density along the direction to the source (including the Galactic absorption); *panel (f)*: $N_{\text{H,p,c}}$, the absorption column density of the partial absorber (representing the absorption column density local to the source; PCFABS in XSPEC); *panel (g)*: $F_{2-10\text{keV}}$, the measured power-law flux in the 2–10 keV energy range not corrected for absorption for the EPIC-pn in units of $10^{-12} \text{ erg s}^{-1} \text{ cm}^{-2}$.

gated the parameter linear correlations, but the small number of available points prevents any significant detection.

3.3.2. Discussion of the results

During the new *XMM-Newton* observation, IGR J11215–5952 displayed a progressively fading lightcurve with a single weak flare occurring at $t \sim 2$ ks and lasting only a few hundreds of seconds (see Fig. 6). The flare was far too faint to detect any significant HR variation. There is an intriguing “dip” in the X-ray emission visible 7.5 ks after the beginning of the observation, but the count-rate was too low to detect any HR variability within the dip itself. As summarized in Fig. 6, our Bayesian analysis technique identified three different time intervals with a decreasing trend in the overall HR. This trend seems to be mostly driven by a softening of the power-law photon index, although the er-

Table 4: Best-fit parameters of the *XMM-Newton* observation of IGR J18410–0535 carried out in 2020 (OBSID 0862410101).

Parameter	Value	unit
N_{H}	$4.06^{+0.17}_{-0.13}$	10^{22} cm^{-2}
Γ	$1.62^{+0.05}_{-0.04}$	
Flux (2–10 keV)	6.17 ± 0.14	$10^{-12} \text{ erg s}^{-1} \text{ cm}^{-2}$

ror bars associated to the best fit parameters in all intervals are relatively large due to the limited statistics of the data. The significant detection of a partial covering component in the spectrum of the source is consistent with the clumpy wind accretion scenario (see Sect. 1), although confirmation through the detection of spectral variability along the rise and decay of brighter flares/outbursts would help us strengthen this conclusion.

3.4. IGR J18410–0535

IGR J18410–0535 was discovered by *ASCA* in 1994 (AXJ1841.0-0536; see Bamba et al. 2001) and associated to the class of the SFXT thanks to the discovery of repeated bright sporadic outbursts by *INTEGRAL* (Rodríguez et al. 2004; Sguera et al. 2006; Walter & Zurita Heras 2007). The optical counterpart was identified as a B1 Ib supergiant at roughly 3.2 kpc (Nespoli et al. 2008). Although the system is thought to host a NS, neither the compact-object pulse period nor the binary orbital period has been firmly measured. During a bright flare caught by *XMM-Newton* in 2011, the source displayed one of the clearest observational evidence to date in favor of clumpy winds playing a major role in the X-ray variability of SgXBs (Bozzo et al. 2011). In 2019, an *XMM-Newton* observation caught the source in the faintest observed state with an upper limit of $2 \times 10^{-14} \text{ erg s}^{-1} \text{ cm}^{-2}$ at 90% confidence level in the 1–10 keV energy band (Ferrigno et al. 2020).

3.4.1. Data analysis and results

Here, we report on a snapshot that *XMM-Newton* performed on IGR J18410–0535 from 2020-10-17 at 20:00:11 to 2020-10-18 at 02:23:31 UT (OBSID 0862410101). The EPIC-pn was operated in full frame, the MOS1 in small window, and the MOS2 in timing mode. The observation was marginally affected by flaring background, so we retained a good time of 14.6 ks out of an elapsed time of 15 ks. The source had an average count rate of 0.4 cts/s in the EPIC-pn 0.5–10 keV band and did not show any appreciable variation of hardness ratio (Fig. 7). We modelled the average spectrum extracted from the three cameras with an absorbed power-law with best fit parameters reported in Table 4.

3.4.2. Discussion of the results

Despite the fact that IGR J18410–0535 is one of the best known SFXTs to have shown the clearest evidence of clumpy wind accretion due to a bright outburst in 2011 (Bozzo et al. 2011), our targeted *XMM-Newton* observations to the source were not able to catch additional bright events. Following the deep upper limit on the source flux that we obtained with an observation in 2019, we could only detect during the additional pointing in 2020 a moderately faint flare in the EPIC lightcurves (see Fig. 7). During the rise and decay of this flare, as well as during the remaining part of the *XMM-Newton* observation, we could not record any significant variation of the HR that could have indicated a change in the spectral parameters and thus provide evidence in

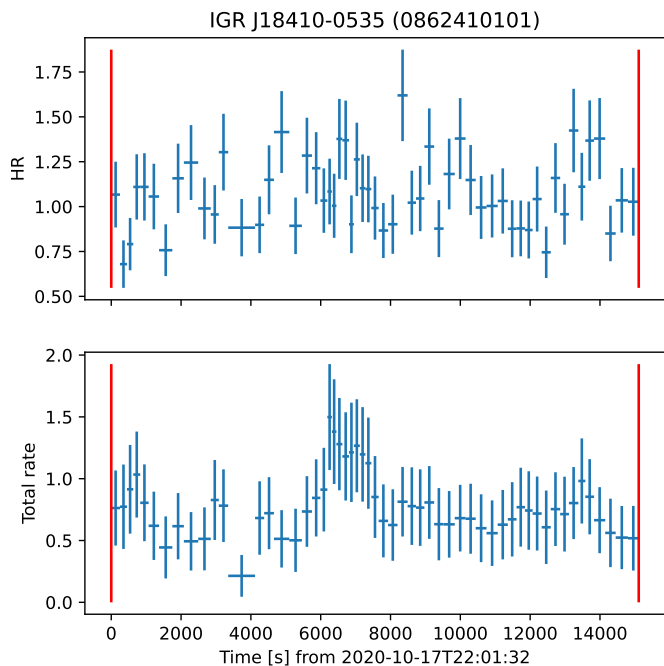


Fig. 7: *Lower panel*: combined EPIC-pn +MOS1 +MOS2 light curve of the 2020 observation of IGR J18410–0535 (OBSID 0862410101) in the 0.5–10 keV energy range. *Upper panel*: hardness ratio between the light curves in the bands 3.5–10 keV and 0.5–3.5 keV rebinned at a minimum S/N of 8. There are no significant variations of the hardness ratio and thus the Bayesian algorithm identified a single time interval for the spectral extraction (marked with red lines and corresponding to the whole observation).

favor of clumpy wind accretion during the low emission state of the source. Given the peculiarity of the 2011 bright outburst, the source clearly deserves further attention and more flares at intermediate luminosity between outburst and quiescence are needed to complete our investigation of the clumpy wind accretion in this source.

3.5. IGR J16393–4643

IGR J16393–4643 is a classical SgXB discovered by *INTEGRAL* in 2004 (Bird et al. 2004) and associated with the previously known X-ray source AX J1639.0-4642 (Sugizaki et al. 2001). The system hosts a ~ 910 s spinning NS (Bodaghee et al. 2006) orbiting around a still poorly known OB companion, and the measured orbital period is of ~ 4.24 d (see Corbet & Krimm 2013, and references therein). The usually heavy extinction measured from X-ray observations in the direction of the source led to the inclusion of this system within the so-called highly obscured X-ray pulsars, a class of objects that has been largely unveiled thanks to *INTEGRAL* observations (see, e.g., Walter et al. 2015, and references therein). IGR J16393–4643 has also shown evidence for a super-orbital modulation, although no firm conclusion has been reached yet (Corbet et al. 2021). The discovery of a CRSF at ~ 29.3 keV led to the determination of the NS magnetic field strength at 2.5×10^{12} G (Bodaghee et al. 2016).

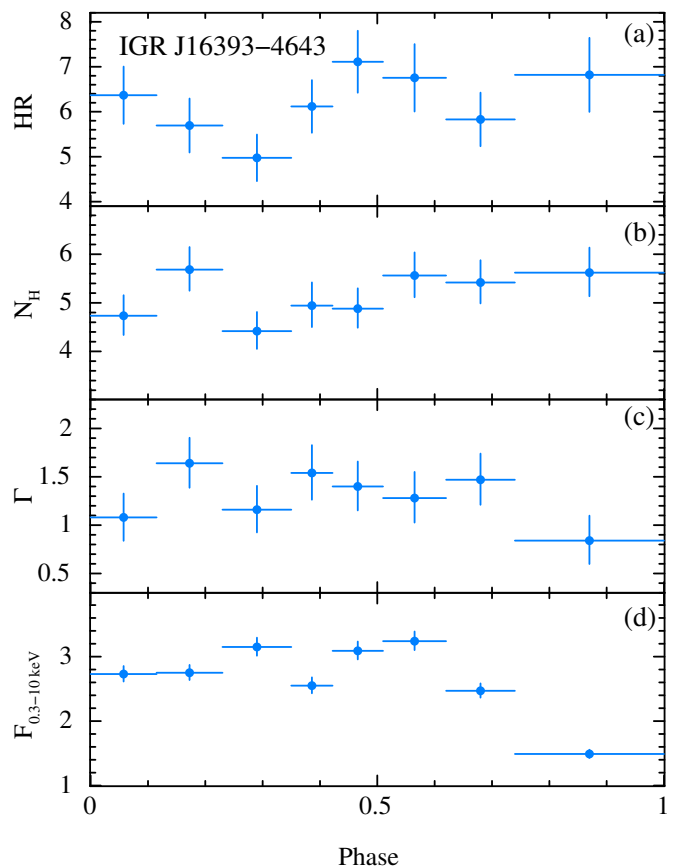


Fig. 8: Same as Fig. 1 but realized for IGR J16393–4643. Here the flux is given in units of 10^{-11} erg cm $^{-2}$ s $^{-1}$.

3.5.1. Data analysis and results

Our monitoring campaign of IGR J16393–4643 was carried out in 2016 with *Swift* /XRT from January to June 2016, with a pace of one 1 ks observation per day (ObsID 34135, for a total of 130 ks) thus covering slightly more than 31 revolutions of the system. A selection of these data (~ 70 ks) have been previously reported by Kabiraj et al. (2020). These authors focused on the properties of the suspected source X-ray eclipse and suggested that this might not be a true eclipse, although it regularly occur at the same orbital phase. Here, we reanalyze the whole data set to carry out an orbital-phase dependent HR-resolved spectral analysis with the main goal of identifying spectral changes that could point toward the existence of large scale structures in the stellar wind around the compact object.

The *Swift* observing logs for IGR J16393–4643 are reported in Table C.3, where we also indicated the orbital phase estimated for each observation by adopting the same ephemerides as in Kabiraj et al. (2020, see Table 1). The equivalent of Fig. 1 but realized in the case of IGR J16393–4643 is shown in Fig. 8a. In order to investigate possible spectral variability in different orbital phase bins, we extracted different source spectra for each of these bins and fit them by using a simple absorbed power-law model. The results are shown in Table 5 and Fig. 8 (panels b–d).

We also checked in the *XMM-Newton* archive suitable observations of IGR J16393–4643 to carry out a HR-resolved spectral analysis aimed at discovering possible spectral variability. The source was observed twice by *XMM-Newton* in 2004 and in

Table 5: Results of the orbital phase-resolved spectral analysis conducted on the *Swift*/XRT data of IGR J16393–4643.

Parameter	Orbital phase							
	0.0–0.115	0.115–0.23	0.23–0.35	0.35–0.422	0.422–0.51	0.51–0.62	0.62–0.74	0.74–1.0
n_{H}	$4.7^{+0.4}_{-0.4}$	$5.7^{+0.5}_{-0.4}$	$4.4^{+0.4}_{-0.4}$	$4.9^{+0.5}_{-0.4}$	$4.9^{+0.4}_{-0.4}$	$5.6^{+0.5}_{-0.4}$	$5.4^{+0.5}_{-0.4}$	$5.6^{+0.5}_{-0.5}$
Γ	$1.1^{+0.2}_{-0.2}$	$1.6^{+0.3}_{-0.3}$	$1.2^{+0.2}_{-0.2}$	$1.5^{+0.3}_{-0.3}$	$1.4^{+0.3}_{-0.2}$	$1.3^{+0.3}_{-0.3}$	$1.5^{+0.3}_{-0.3}$	$0.8^{+0.3}_{-0.2}$
$F_{0.3-10\text{keV}}$	$2.7^{+0.1}_{-0.1}$	$2.7^{+0.1}_{-0.1}$	$3.2^{+0.1}_{-0.1}$	$2.6^{+0.1}_{-0.1}$	$3.1^{+0.1}_{-0.1}$	$3.2^{+0.2}_{-0.1}$	$2.5^{+0.1}_{-0.1}$	$1.5^{+0.1}_{-0.1}$
Cstat/d.o.f.	452.9/515	521.0/506	492.3/515	434.7/477	409.3/495	469.6/507	415.3/526	442.1/546

Notes. We report the measured value of the absorption column density (N_{H} , in units of 10^{23} cm^{-2}), the power-law photon index (Γ), and the 0.3–10 keV flux (not corrected for absorption) in units of $10^{-11} \text{ erg cm}^{-2} \text{ s}^{-1}$.

2010. However, both observations are not suitable to our goal. The observation in 2004 is relatively short (~ 8 ks) and it shows 8 peaks and valleys corresponding to the source pulse period (Bodagheer et al. 2006). There is no flaring behavior that could be analyzed to look for HR variations. During the slightly longer observation carried out in 2010 (~ 10 ks), the source was a factor of ≥ 10 fainter and the lightcurve does not show any flaring behavior that is bright enough to carry out a meaningful HR-resolved spectral analysis (see also Pradhan et al. 2018).

3.5.2. Discussion of the results

Our detailed study of the source orbital phase-resolved HR and spectral properties extend and complete the previous work from Kabiraj et al. (2020). We analyzed all XRT data of our monitoring campaign with a uniform technique exploited for all the SgXBs in this paper (to facilitate a direct comparison) and computed the HR value of the folded XRT data over the source orbital period in 8 phase bins containing virtually the same number of photons. The spectra extracted in each of these bins could be well fit with a simple absorbed powerlaw model, and the plot of these parameters (as well as the HR) as a function of the orbital phase in Fig. 8 does not show any prominent variability. There is a potentially interesting V-shaped feature in the profile of the source flux between phases 0.3–0.5, but such feature does not seem to be connected with either a significant change of the powerlaw slope or a variation of the local column density. The source is heavily obscured along the entire orbit ($N_{\text{H}} \gg 10^{23} \text{ cm}^{-2}$) and the limited band-pass of the XRT energy coverage did not reveal significant variations of the HR (given also the relatively large associated error bars).

The relatively sharp drop of the source X-ray flux around phase 0.75–1.0 corresponds to the suspected eclipse studied also by Kabiraj et al. (2020) and Islam et al. (2015). In agreement with their results, our analysis also evidences that, despite the decrease by a factor of ≥ 2 in the source flux, the other spectral parameters did not show at this particular orbital phase a dramatic variation compared to other phases. We recorded a flattening of the powerlaw photon index that, in principle, is expected in case of an X-ray eclipse. However, this is not accompanied by a drop in the local absorption column density. Such drop is expected because during the eclipse the source of X-rays is hidden from the direct view of the observer who is looking rather to the remaining diffuse fluorescence emission of the X-rays from the occulted NS onto the surrounding wind material spread all around the binary system (see, e.g., Bozzo et al. 2009, and references therein).

The XRT data are thus raising concerns against the interpretation of the drop in flux at phases 0.75–1.0 as an X-ray eclipse,

but the statistics is far too low to allow a deeper analysis. Kabiraj et al. (2020) proposed that this drop in flux could be caused by a grazing eclipse and absorption of the X-rays in the stellar corona. At present, however, alternative possibilities cannot be excluded. In the context of the corotating interaction regions, there could be the intriguing possibility that the obscuration is due to one of these large structures that is tilted away from the plane of the NS orbit and attenuate the X-ray emission along the line of sight to the observer mainly through scattering with a non-measurable enhancement of photoelectric absorption as for the grazing eclipse (this idea was put forward already in Bozzo et al. 2016). Interestingly, the source has also displayed evidence for an at least transitory super-orbital period, which origin could be also related to corotating interaction regions (Corbet et al. 2021). The peculiar orbital phase 0.75–1.0 of IGR J16393–4643 definitively deserves a dedicated observation with larger effective area instruments (as the EPIC cameras on-board *XMM-Newton*) able to eventually detect emission/absorption lines, providing details about the physical conditions of the material causing obscuration, as well as revealing modest variations of the spectral parameters that could go undetected due to the limited statistics of the *Swift*/XRT data.

3.6. XTE J1855–026

XTE J1855–026 was discovered by the *RXTE* satellite in 1998 (Corbet et al. 1999) and it is known to host a ~ 361 s spinning NS orbiting every 6.1 d a BN0.2 Ia supergiant star located at roughly 10 kpc (see González-Galán 2015, and references therein). The optical companion was identified thanks to the refined *Swift* position obtained with an arcsec level accuracy (Romano et al. 2008). XTE J1855–026 is known to be eclipsing (see Falanga et al. 2015; Coley et al. 2015, for the most updated source ephemerides) and it has long been classified as a classical SgXB, although its behavior is partly anomalous compared to other objects of this class due to the emission of sporadic bright X-ray outbursts. These have been observed a few times with *INTEGRAL* and *Swift* (see, e.g., Watanabe et al. 2010; Krimm et al. 2012, and references therein).

3.6.1. Data analysis and results

We report on a detailed analysis of the yet unpublished *Swift* data (see Table C.4) collected during the outburst observed in 2011 (Krimm et al. 2012). This is the only outburst for which data in the soft X-ray domain ($\lesssim 1-2$ keV) are available.

XTE J1855–026 triggered the BAT (image trigger 503434) on 2011 September 18 at 10:07:28.6 UT (T_0 , MJD 55822.42186, orbital phase 0.61); *Swift* slewed to the target so that the narrow-

Table 6: Spectral analysis conducted on the *Swift* observations of XTE J1855–026.

Spectra (model)	Time range (s) since trigger	N_{H} (10^{23} cm^{-2})	Γ	E_{cut} (keV)	$F_{15-50 \text{ keV}}$ ($\times 10^{-9}$)	$F_{0.3-10 \text{ keV}}$ ($\times 10^{-10}$)	$\chi^2/\text{d.o.f.}$ Cstat/d.o.f.
BAT evt (PL)	–239–960	-	2.48 ± 0.09	-	2.27 ± 0.08	-	30.90/24
BAT evt (CPL)	–239–960	-	$0.48^{+0.58}_{-0.64}$	16^{+9}_{-3}	2.31 ± 0.08	-	16.63/23
BAT DPH1 (PL)	1504–1804	-	$2.45^{+0.15}_{-0.14}$	-	1.88 ± 0.15	-	26.08/4
BAT DPH2 (PL)	1804–2104	-	$2.44^{+0.24}_{-0.21}$	-	1.32 ± 0.14	-	6.81/4
BAT DPH3 (PL)	2104–2382	-	$2.16^{+0.18}_{-0.17}$	-	1.49 ± 0.14	-	9.98/4
WT1 (PL)	1510–1627	$1.8^{+0.5}_{-0.4}$	$0.4^{+0.4}_{-0.4}$	-	-	$9.9^{+0.8}_{-0.7}$	279/380
PC1 (PL)	1629–2376	$1.2^{+0.3}_{-0.2}$	$-0.2^{+0.3}_{-0.3}$	-	-	$7.2^{+0.6}_{-0.5}$	260/307
WT2 (PL)	6788–8160	$4.0^{+0.9}_{-0.7}$	$1.3^{+0.6}_{-0.5}$	-	-	$1.8^{+0.2}_{-0.2}$	240/298
PC2 (PL)	6795–8154	$3.0^{+1.2}_{-0.8}$	$0.6^{+0.7}_{-0.6}$	-	-	$1.3^{+0.2}_{-0.1}$	162/144
WT3 (PL)	11708–11740	$0.8^{+0.9}_{-0.3}$	$0.7^{+0.9}_{-0.6}$	-	-	$4.4^{+1.1}_{-0.9}$	62/85
DPH1 + WT1 (CPL)	-	0.9 ± 0.1	$-0.46^{+0.09}_{-0.10}$	10 ± 1	$2.2^{+0.1}_{-0.2}$	$10.1^{+1.3}_{-0.8}$	355.49/389
DPH2,3 + PC1 (CPL)	-	0.6 ± 0.2	$-0.96^{+0.38}_{-0.35}$	9^{+2}_{-1}	$1.5^{+0.1}_{-1.2}$	$7.1^{+0.1}_{-7.0}$	336.19/322
DPH1 + WT1 (CPL+Fe)	-	0.8 ± 0.1	$-0.45^{+0.09}_{-0.10}$	10 ± 1	$2.2^{+0.1}_{-0.2}$	$9.9^{+0.5}_{-0.6}$	347.62/389
DPH2,3 + PC1 (CPL+Fe)	-	0.6 ± 0.2	$-0.11^{+0.10}_{-0.09}$	13^{+3}_{-1}	$1.44^{+0.04}_{-1.44}$	≤ 5.8	276.45/322

Notes. The power-law model is indicated with PL, the exponential cut-off with CPL. We report the measured value of the absorption column density (N_{H} , in units of 10^{23} cm^{-2}), the power-law photon index (Γ), the cut-off energy (in keV) and the fluxes in the 15–50 keV energy band from BAT (in units of $10^{-9} \text{ erg cm}^{-2} \text{ s}^{-1}$), and in the 0.3–10 keV energy band from XRT (not corrected for absorption) in units of $10^{-10} \text{ erg cm}^{-2} \text{ s}^{-1}$.

field instruments started observing at $T_0 + 1510 \text{ s}$ (see Table C.4). The BAT event data were analysed using the standard BAT analysis software within FTOOLS. Mask-tagged BAT light curves, covering the time range $T_0 - 239$ to $T_0 + 963 \text{ s}$, were created in the standard energy bands (15–25, 25–50, 50–100, 100–350 keV), and rebinned to fulfill at least one of the following conditions: reaching a signal-to-noise ratio (S/N) of 5 or bin length of 10 s. The light curves of the first orbit of data are shown in Fig. 9. A mask-weighted spectrum was also extracted from the events collected during the first orbit; we applied an energy-dependent systematic error vector to the data and created response matrices with BATDRMGEN using the latest spectral redistribution matrices. This spectrum, when fit in the energy range 15–70 keV with a simple power law, yields a photon index of 2.48 ± 0.15 ($\chi^2/\text{d.o.f.} = 30.90/24$) and a 15–50 keV flux of $(2.27 \pm 0.08) \times 10^{-9} \text{ erg cm}^{-2} \text{ s}^{-1}$ (see Table 6). This fit, however, shows residuals that indicate a curvature, so a fit with a cut-off power-law model was also made, yielding a photon index of $0.48^{+0.58}_{-0.64}$ and a cut-off energy $E_{\text{cut}} = 16^{+9}_{-3} \text{ keV}$ ($\chi^2/\text{d.o.f.} = 16/23$). We note that there are no XRT data simultaneous with this BAT spectrum. The XRT light curve, split in 3 snapshots, starts at $T_0 + 1510 \text{ s}$ and shows a dynamic range of ~ 20 in $\sim 6 \text{ ks}$ (0.3–10 keV, see Fig. 9). The hardness ratio, calculated in the 0.3–4 and 4–10 keV bands is shown in Fig. 10. XRT spectra were extracted in each observing mode and each of the snapshots that comprise the data set, thus obtaining three window timing (WT) and two photon counting (PC) spectra, and were fit with the a simple absorbed power-law model and Cash statistics. A summary of the spectral results is shown in Table 6.

BAT survey data products, in the form of detector plane histograms (DPH), are also available, and were analysed with the standard FTOOLS software. Since BAT survey data are accumulated on-board with typical integration times of 300 s, pairing simultaneous BAT survey data with the XRT ones is not straightforward. Therefore we extracted spectra (6 energy bins) that most closely matched the XRT data: *i*) DPH1 from $T_0 + 1504 \text{ s}$ to $T_0 + 1804 \text{ s}$; *ii*) DPH2 in the time range $T_0 + 1804$ –2104 s;

iii) DPH3 in the time range $T_0 + 2104$ –2382 s. Each BAT spectrum was fit with a simple power-law model (results in Table 6). In order to ensure the closest to simultaneity, we chose to fit the following BAT and XRT groups: *a*) DPH1+WT1, *b*) DPH2+DPH3+PC2. When fitting these BAT and XRT spectra together, a constant needs to be used to model both the difference of exposure and the non strict simultaneity. Furthermore, the XRT spectra are fit by minimizing Cash statistics, while the BAT ones with χ^2 statistics.

A fit to the DPH1+WT1 pair with an absorbed power-law model resulted in residuals suggesting a spectral curvature, so we also performed a fit using an absorbed cut-off power law. This yielded a $N_{\text{H}} = 0.9 \pm 0.1 \times 10^{23} \text{ cm}^{-2}$, a photon index of $-0.46^{+0.09}_{-0.10}$ and a cut-off energy $E_{\text{cut}} = 10 \pm 1 \text{ keV}$ (inter-calibration constants $C_{\text{DPH1}} = 1$ fixed and $C_{\text{WT1}} = 2.6^{+0.4}_{-0.3}$). This is reported in Table 6. The addition of an Iron line, represented by a Gaussian model with energy $\sim 6.4 \text{ keV}$, yields a continuum fit with $N_{\text{H}} = 0.8 \pm 0.1 \times 10^{23} \text{ cm}^{-2}$, a photon index of $-0.45^{+0.09}_{-0.10}$ and a cut-off energy $E_{\text{cut}} = 10 \pm 1 \text{ keV}$ (inter-calibration constants $C_{\text{DPH1}} = 1$ (fixed) and $C_{\text{WT1}} = 2.4^{+0.4}_{-0.3}$), while the line is characterised by a centroid energy $E_{\text{Fe}} = 6.4^{+0.8}_{-0.7} \text{ keV}$ and a width consistent with zero ($< 1.52 \text{ keV}$) and an equivalent width $\text{EW} = 0.18^{+0.24}_{-0.17} \text{ keV}$ (Fig. 11).

Similarly, a fit to the DPH2+DPH3+PC2 group with an absorbed power-law model indicated the presence of a possible spectral curvature in the residuals. An absorbed cut-off power law fit yielded a $N_{\text{H}} = 0.6 \pm 0.2 \times 10^{23} \text{ cm}^{-2}$, a photon index of $-0.96^{+0.38}_{-0.35}$, and a cut-off energy $E_{\text{cut}} = 9^{+2}_{-1} \text{ keV}$ (inter-calibration constants $C_{\text{DPH2}} = 1$ (fixed), $C_{\text{DPH3}} = 1.2^{+0.2}_{-0.1}$, and $C_{\text{PC1}} = 3.8^{+1.4}_{-0.9}$). This is reported in Table 6. The addition of an Iron line, represented by a Gaussian model with energy $\sim 6.4 \text{ keV}$, yields a continuum fit with $N_{\text{H}} = 0.6 \pm 0.2 \times 10^{23} \text{ cm}^{-2}$, a photon index of $-0.11^{+0.10}_{-0.09}$ and a cut-off energy $E_{\text{cut}} = 13^{+3}_{-1} \text{ keV}$ (inter-calibration constants $C_{\text{DPH1}} = 1$ (fixed) $C_{\text{DPH3}} = 1.2 \pm 0.1$, and $C_{\text{PC1}} = 1.3^{+0.5}_{-0.3}$), while the line is characterised by a centroid energy $E_{\text{Fe}} = 6.4 \pm 0.2 \text{ keV}$, a width of $0.85^{+0.14}_{-0.11} \text{ keV}$ and $\text{EW} \gg 1 \text{ keV}$ (Fig. 12).

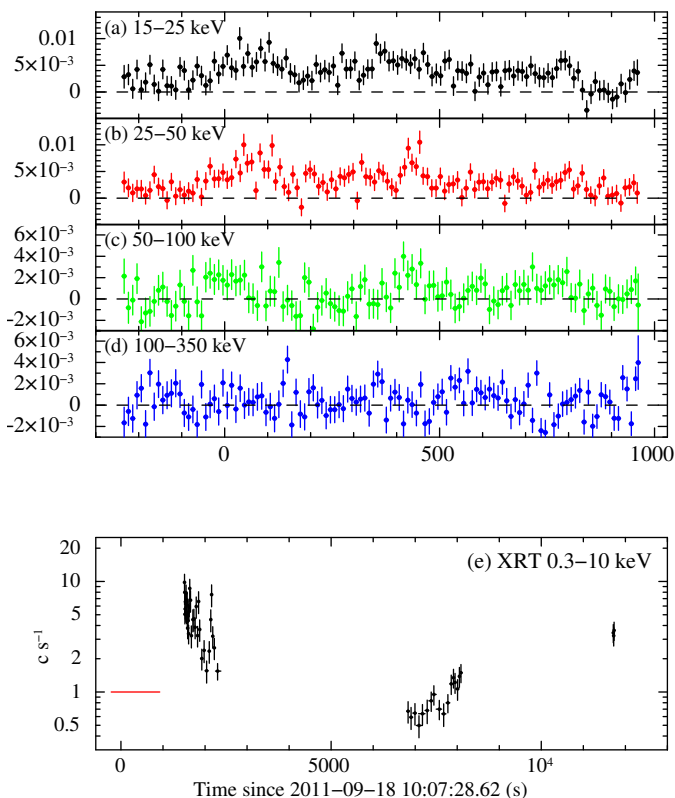


Fig. 9: Light curves of the 2011 September 18 outburst of XTE J1855-026 caught by BAT and XRT. *Panels (a–d)*: BAT light curves (c s^{-1} , at 10 s binning); *panel (e)*: XRT light curve (0.3–10 keV c s^{-1}); the horizontal line marks the time where BAT event data were collected. Note the different scale in the x-axis.

3.6.2. Discussion of the results

The outburst of the source in 2011 was the only one where the broad-band emission from XTE J1855-026 could be studied combining data from a large field of view instrument (*Swift*/BAT) with those collected in the soft X-rays by a focused telescope (*Swift*/XRT). Although the XRT lightcurve during the outburst is fragmented due to the observational strategy of the satellite, the coverage of the outburst allows us to study possible changes in the spectral properties of the source X-ray emission from the onset of the event down to the return to the usual emission level.

We see from Fig. 10 that XRT pointed the source about 1.5 ks after the onset of the outburst. The instrument recorded a progressive rise of the absorption column density, starting at $\lesssim 2 \times 10^{22} \text{ cm}^{-2}$ (WT1 and PC1 data in Table 6) and reaching up to $4 \times 10^{22} \text{ cm}^{-2}$ a few ks after the beginning of the monitoring (WT2 and PC2 data in Table 6). Interestingly, XRT also recorded a new drop of the absorption column density down to $0.8 \times 10^{22} \text{ cm}^{-2}$ about 11 ks after the onset of the event when the flux decay was interrupted by a new brightening of the source (WT3 data in Table 6). This behavior resembles what is typically observed in clumpy wind accreting systems, but in the case of the 2011 outburst of XTE J1855-026, we have likely missed the initial increase in the local absorption column density as the XRT only began observing about 1.5 ks after the onset of the event. Nevertheless, we clearly detect the progressive increase of the local absorption column density during the decay of the

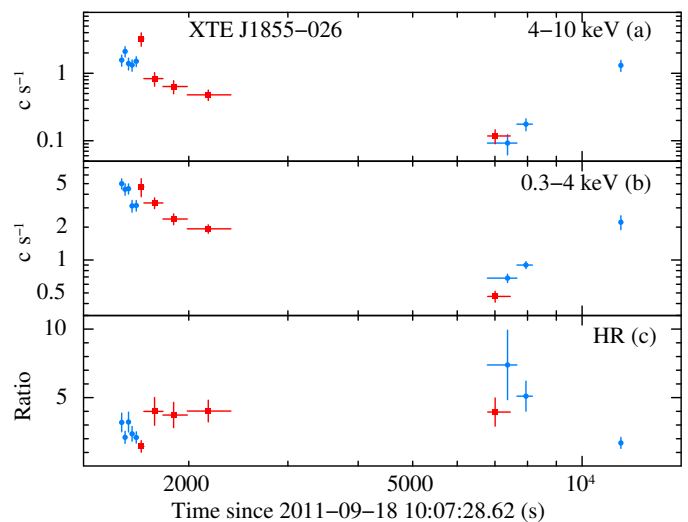


Fig. 10: *Panel (a)*: XRT hard band light curve (4–10 keV c s^{-1}); *panel (b)*: soft band light curve (0.3–4 keV c s^{-1}); *panel (c)*: hardness ratio (4–10 keV/0.3–4 keV). WT data are shown in blue, PC data in red.

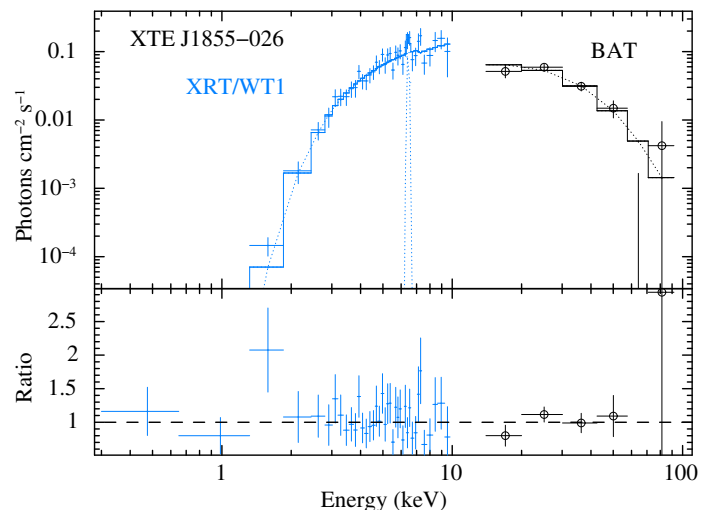


Fig. 11: Spectroscopy of the 2011 September 18 outburst of XTE J1855-026. Top panel: unfolded spectra of the nearly-simultaneous XRT/WT1 data (blue crosses) and BAT DPH1 data (empty black circles) fit with an absorbed cut-off power-law model. Bottom panel: data/model ratio of the fit.

outburst associated to the fading of the source and the diminishing effect of the photoionization onto the clumpy wind. The drop of the local absorption column density about 11 ks after the onset of the flare further strengthens this conclusion as it can be ascribed to the renewed effect of the photoionization when the source underwent a second (fainter) brightening.

The onset of the outburst up to 1.5 ks was observed by *Swift* only with the BAT. The hard X-ray spectrum above 15 keV could be described reasonably well with a simple power-law and the measured photon index is compatible with that recorded during the outbursts observed with the hard X-ray imager IBIS/ISGRI on-board *INTEGRAL* (Watanabe et al. 2010). However, the BAT data showed evidence for a possible curvature in the hard en-

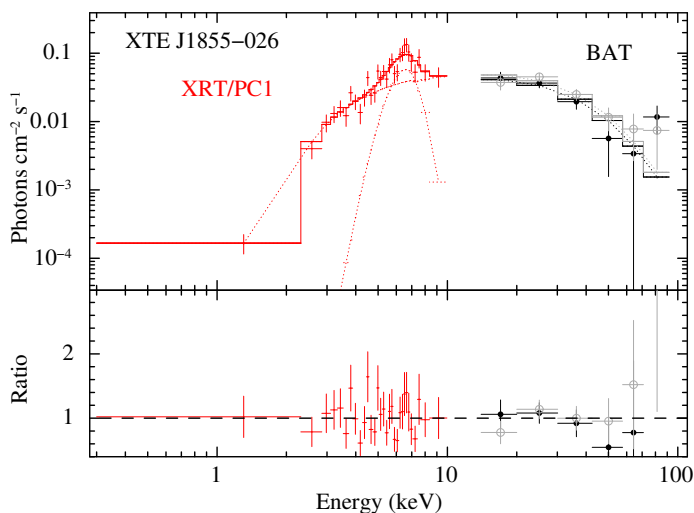


Fig. 12: Spectroscopy of the 2011 September 18 outburst of XTE J1855–026. Top panel: unfolded spectra of the simultaneous XRT/PC1 data (red crosses), the BAT DPH2 data in black (filled circles) and the BAT DPH3 data in grey (empty circles) fit with an absorbed cut-off power-law model. Bottom panel: data/model ratio of the fit.

ergy spectrum, with a cut-off energy at about 16 keV. When the XRT data are combined with the (quasi-)simultaneous BAT survey data during the later stages of the outburst development (data DPH1+WT1 and DPH2,3+PC1 in Table 6), the value of the measured curvature slightly decreases toward ~ 10 keV, although the associated uncertainties remained quite large due to the limited statistics of the data. Such curvature is rather ubiquitous in accreting SgXBs (see, e.g. Walter et al. 2015, and references therein) and was also reported previously in the case of XTE J1855–026 (Corbet et al. 1999). In the broadband fit of the XRT+BAT data, we find evidence for the presence of an iron line at a centroid energy of 6.4 keV. Although the statistics of the XRT data in the energy range of the iron line is limited, such feature is expected in the case of an SgXB. The iron line at 6.4 keV is commonly observed in wind-fed systems, due to the fluorescence of the X-rays from the accreting compact object onto the surrounding stellar winds (see, e.g. Torrejón et al. 2010; Giménez-García et al. 2016, for recent reviews). Iron lines with compatible parameters as those measured by XRT were already reported in the case of XTE J1855–026 by Devasia & Paul (2018) using *Suzaku* data.

Given its classification as a classical SgXBs and the presence of peculiar bright short outbursts similar to those of the SFXTs, XTE J1855–026 remains today an intriguing object that has likely not drawn sufficient attention from the community. It remains relatively poorly studied, as no detailed orbital monitoring in the soft X-rays has been carried out yet and we are missing sufficiently long exposure observations with the large area X-ray instruments (as the EPIC cameras) to probe possible emission/absorption lines in the high energy domain to investigate the properties of the stellar wind material within the binary. The evidence reported in this paper about the clumpy wind accretion in XTE J1855–026 provides good perspectives to renew the interest in this system.

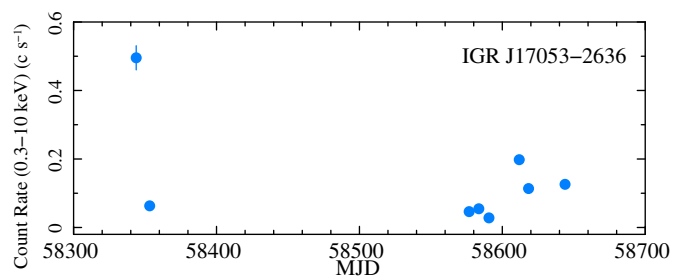


Fig. 13: Long-term light curve of IGR J17503–2636 as measured by *Swift* /XRT. For completeness, we included the XRT observations already published in our previous paper on the source (MJD 58343 and 58333, Ferrigno et al. 2019).

3.7. IGR J17503–2636

IGR J17503–2636 is an SFXT discovered by *INTEGRAL* in 2018 (Chenevez et al. 2018). The source underwent a bright X-ray flare lasting several hours before rapidly going back to a quiescent emission level (the measured dynamical range in the X-ray domain is of ~ 300 ; see Chakrabarty et al. 2018a,b; Ferrigno et al. 2019). The optical counterpart was tentatively identified as a heavily obscured supergiant located beyond the Galactic center (Masetti et al. 2018), although these findings require further consolidation (McCullum et al. 2018). The *NuSTAR* data collected shortly after the discovery showed evidence for the presence of a cyclotron scattering feature in the broad-band spectrum of the source, suggesting that the compact object accreting in this system is a NS endowed with a magnetic field strength of $\sim 2 \times 10^{12}$ G (Ferrigno et al. 2019).

3.7.1. Data analysis and results

We report on our *Swift*/XRT follow-up campaign until up to about one year after the discovery of the source, spanning from April to June 2019 (with a pace of one 5 ks observation per week, ObsID 10980), and not yet published elsewhere. As the orbital period of the source is not known, we could only consider here the long term evolution of the source X-ray emission.

The summary of the available XRT observations of IGR J17503–2636 is provided in Table C.5. In the table we also report the measured flux of each XRT observation, together with the best fit parameters; all spectra of IGR J17503–2636 could be fit well with a simple absorbed power-law model. We also included for completeness in the table one ~ 2 ks serendipitous observation in the *Swift* archive (MJD 56224) preceding the discovery where the source and not yet published elsewhere. During this pointing, the source was found in a low state (the measured count rate is $5.2 \pm 0.7 \times 10^{-1} \text{ c s}^{-1}$ corresponding to a 0.3–10 keV flux of $0.5^{+0.3}_{-0.2} \times 10^{-11} \text{ erg cm}^{-2} \text{ s}^{-1}$). The long-term X-ray light curve of IGR J17503–2636 as measured by XRT is shown in Fig. 13.

3.7.2. Discussion of the results

Our XRT monitoring campaign of IGR J17503–2636 demonstrates that the source behaves as most SFXTs, remaining at a fairly faint quiescent level for most of their lifetime outside rare and sporadic outbursts (so far only one outburst has been recorded). The source shows a rather stable spectral energy distribution over time during the low level emission state, as ob-

served in several SFXTs (see, e.g., [Walter et al. 2015](#), and references therein). As the source was regularly detected during each of the performed XRT pointing at a flux of $\sim 10^{-11}$ erg s $^{-1}$ cm $^{-2}$ or higher, our campaign seems to invalidate the tentative conclusion presented by [Ferrigno et al. \(2019\)](#) according to which the source is a faint SFXT due to its particularly high distance beyond the Galactic center (this was proposed to explain why no previous outbursts were ever detected from the source by the large field of view instruments on-board *INTEGRAL* and/or *Swift*).

The measured XRT fluxes correspond to a luminosity of roughly $\sim 10^{35}$ erg s $^{-1}$ at 10 kpc and the quiescent luminosity of several SFXTs has been measured to be as low as 10^{32} erg s $^{-1}$. The archival XRT observation that we reported here for the first time also confirmed that the source was already active at a similar flux level in 2012, about 6 years before the discovery of the first outburst by *INTEGRAL*. The reason why no previous outbursts have ever been detected before 2018 remains to be explained. The intrinsic fragmentation of the XRT light curves (due to the pointing strategy of the satellite) did not allow us to study the SFXT typical behavior of flaring also at the lowest emission states, during which evidence of the clumpy wind accretion are commonly found (see Sect. 1). For all these reasons, the source certainly deserves further observations to find clearer evidence of clumpy wind accretion and measure possible changes in the cyclotron line properties that could be associated with variations in the NS magnetic field configuration.

4. Conclusions

We reported in this paper on the outcomes from our concluded observational campaigns of several classical SgXBs and SFXTs with both *Swift* and *XMM-Newton*. The goals of the data we collected were mainly to study structures in the stellar winds surrounding the compact objects in these systems, revealing details of the still highly debated macro-clumps, as well as other larger structures. In the field of macro-clumping, the results presented here complement those reported in our previous papers, while the longer-term XRT observational campaigns were reported here for the first time.

As a general conclusion, we found that the observational strategies set to study structures in the massive star winds with both *XMM-Newton* and *Swift* have been so far successful, with the former focusing on the shorter term variability associated with the accretion of clumps (few thousands seconds to hours) and the latter on the longer time-scale variability (few to several days) associated with different orbital phases of these systems and driven by larger stellar wind structures (as accretion and photoionization wakes, CIRs, and accretion streams).

Short *XMM-Newton* observations had been already exploited in a number of previous papers from our group and although we had been able to report in the past on significantly brighter flares than those described here, we could still advance the census of these kind of events from both classical SgXBs and SFXTs. In particular, the observation of the classical SgXB 4U 1907+09 allowed us to provide interesting evidence about how the encounter between the NS and a clump can affect the accretion process beyond the variations of the continuum emission and absorption column density studied before. The lack of spectral variability in the flares recorded from IGR J18410–0535 and IGR J11215–5952 increases the statistics of events that seem to occur without the interventions of clumps, likely triggered by additional mechanisms as the centrifugal and magnetic gating or the settling accretion regime. The lack of spectral variability is

particularly puzzling in the case of IGR J11215–5952 where the observed flare by *XMM-Newton* reaches the previously reported threshold of a few cts s $^{-1}$ above which variations are expected ([Bozzo et al. 2017b](#)).

We also exploited in this paper XRT and BAT observations of XTE J1855–026, caught during a rare bright outburst in 2011 (and yet unpublished). We could study for the first time the source broad band emission with high sensitivity and looked for possible spectral features and variability during the event. Although the source displayed a remarkable dynamic range in its X-ray luminosity, our analysis could not reveal any significant spectral variability. This source remains so far poorly studied and understood, being characterized by an intermediate behavior between classical SgXBs and SFXTs.

The study of orbital-phase spectral variability reported here for the first time with *Swift*/XRT has undoubtedly helped us understanding which among the observed sources are more likely to display measurable periodic spectral changes along their revolutions. In the case of 4U 1907+09, our XRT campaign confirmed previous findings about the peculiar changes in the source flux, continuum slope, and absorption column density at different orbital phases, but we were able to extend literature studies exploiting the lower energy band-pass of XRT. This allowed us to reveal even more extreme variations especially of the local absorption column density to the source. Thanks to the XRT coverage at these low energies, we were able to reveal a completely analogous behavior in IGR J19140+0951, and proposed for this object a similar scenario as that studied already in much better details for 4U 1907+09, involving the presence of a non-negligible eccentricity and a massive structure moving with the NS, likely a gas stream. No particularly striking variability has instead been observed from the orbital monitoring of IGR J16393–4643. This source is relatively faint even for XRT and although it is possible that some variability has gone undetected within the measured uncertainties of the different spectral parameters, we can definitively rule out prominent spectral changes as those measured from either 4U 1907+09 or IGR J19140+0951. In the case of the SFXT IGR J17503–2636, we could not study spectral variability along the different orbital phases as the system orbital period is not known yet. Our XRT observations revealed, however, that the source remained relatively stable in terms of X-ray flux and spectral energy distribution over time. Having followed the source up to nine months after its initial discovery in 2018 and having reported its detection in an archival XRT observation dating back in 2012, we consider that it is reasonable to assume that the source is displaying a low persistent luminosity with rare outbursts (only one detected so far) as it is common for the SFXTs. This further strengthens the previous conclusions about the nature of this source.

Acknowledgements. The data underlying this article are publicly available from the *XMM-Newton*, *RXTE*, *Swift*, and *NuSTAR* archives. The full chain of the analysis of the *XMM-Newton* and *INTEGRAL* data is available in the form of a python Notebook that can be run in a dockerized environment for [4U J1907+097](#), [IGR J18410–0535](#), and [IGR J11215–5952](#). We thank the anonymous referee for detailed comments that helped us improve the paper. The *Swift* data of our monitoring campaigns were obtained through contract ASI-INAF I/004/11/5 (PI P. Romano). PR and EB acknowledge financial contribution from contract ASI-INAF I/037/12/0. This work made use of data supplied by the UK Swift Science Data Centre at the University of Leicester (see [Evans et al. 2007, 2009](#)) and by the multi-messenger online data analysis (*MMODA*) platform at the University of Geneva (see [Neronov et al. 2021](#)). CF is grateful to Dr. Volodymyr Savchenko for providing assistance with *MMODA* and for sharing the tuning of *sextractor* to *IBIS* imaging.

References

- Arnason, R. M., Papei, H., Barmby, P., Bahramian, A., & Gorski, M. D. 2021, *MNRAS*, 502, 5455
- Bamba, A., Yokogawa, J., Ueno, M., Koyama, K., & Yamauchi, S. 2001, *PASJ*, 53, 1179
- Barret, D., Lam Trong, T., den Herder, J.-W., et al. 2016, in *Society of Photo-Optical Instrumentation Engineers (SPIE) Conference Series*, Vol. 9905, *Space Telescopes and Instrumentation 2016: Ultraviolet to Gamma Ray*, ed. J.-W. A. den Herder, T. Takahashi, & M. Bautz, 99052F
- Bertin, E. & Arnouts, S. 1996, *A&AS*, 117, 393
- Bird, A. J., Barlow, E. J., Bassani, L., et al. 2004, *ApJ*, 607, L33
- Bodaghee, A., Tomsick, J. A., Fornasini, F. M., et al. 2016, *ApJ*, 823, 146
- Bodaghee, A., Walter, R., Zurita Heras, J. A., et al. 2006, *A&A*, 447, 1027
- Bozzo, E., Bernardini, F., Ferrigno, C., et al. 2017a, *A&A*, 608, A128
- Bozzo, E., Ducci, L., & Falanga, M. 2021, *MNRAS*, 501, 2403
- Bozzo, E., Falanga, M., & Stella, L. 2008, *ApJ*, 683, 1031
- Bozzo, E., Giunta, A., Cusumano, G., et al. 2011, *A&A*, 531, A130
- Bozzo, E., Kuulkers, E., Postel, A., et al. 2017b, *The Astronomer's Telegram*, 10645
- Bozzo, E., Oskinova, L., Feldmeier, A., & Falanga, M. 2016, *A&A*, 589, A102
- Bozzo, E., Romano, P., Ducci, L., Bernardini, F., & Falanga, M. 2015, *Advances in Space Research*, 55, 1255
- Bozzo, E., Romano, P., Ferrigno, C., et al. 2013a, *A&A*, 556, A30
- Bozzo, E., Romano, P., Ferrigno, C., Esposito, P., & Mangano, V. 2013b, *Advances in Space Research*, 51, 1593
- Bozzo, E., Stella, L., Ferrigno, C., et al. 2010, *A&A*, 519, A6
- Bozzo, E., Stella, L., Israel, G., Falanga, M., & Campana, S. 2009, in *American Institute of Physics Conference Series*, Vol. 1126, *American Institute of Physics Conference Series*, ed. J. Rodriguez & P. Ferrando, 319–321
- Burrows, D. N., Hill, J. E., Nousek, J. A., et al. 2005, *Space Sci. Rev.*, 120, 165
- Chakrabarty, D., Jonker, P. G., & Markwardt, C. B. 2018a, *The Astronomer's Telegram*, 11990, 1
- Chakrabarty, D., Jonker, P. G., & Markwardt, C. B. 2018b, *The Astronomer's Telegram*, 11991, 1
- Chenevez, J., Jaisawal, G., Kuulkers, E., et al. 2018, *The Astronomer's Telegram*, 11952, 1
- Clavel, M., Tomsick, J. A., Hare, J., et al. 2019, *ApJ*, 887, 32
- Coley, J. B., Corbet, R. H. D., & Krimm, H. A. 2015, *ApJ*, 808, 140
- Corbet, R. H. D., Coley, J. B., Krimm, H. A., Pottschmidt, K., & Roche, P. 2021, *ApJ*, 906, 13
- Corbet, R. H. D., Hannikainen, D. C., & Remillard, R. 2004, *The Astronomer's Telegram*, 269, 1
- Corbet, R. H. D. & Krimm, H. A. 2013, *ApJ*, 778, 45
- Corbet, R. H. D., Markwardt, C. B., & Tueller, J. 2007, *ApJ*, 655, 458
- Corbet, R. H. D., Marshall, F. E., Peele, A. G., & Takeshima, T. 1999, *ApJ*, 517, 956
- Cox, N. L. J., Kaper, L., & Makiem, M. R. 2005, *A&A*, 436, 661
- Şahiner, Ş., Inam, S. Ç., & Baykal, A. 2012a, *MNRAS*, 421, 2079
- Şahiner, Ş., Inam, S. Ç., & Baykal, A. 2012b, *MNRAS*, 421, 2079
- D'Ai, A., La Parola, V., Cusumano, G., et al. 2011, *A&A*, 529, A30
- Devasia, J. & Paul, B. 2018, *Journal of Astrophysics and Astronomy*, 39, 7
- Doroshenko, V., Santangelo, A., Ducci, L., & Klochkov, D. 2012, *A&A*, 548, A19
- Evans, P. A., Beardmore, A. P., Page, K. L., et al. 2009, *MNRAS*, 397, 1177
- Evans, P. A., Beardmore, A. P., Page, K. L., et al. 2007, *A&A*, 469, 379
- Falanga, M., Bozzo, E., Lutovinov, A., et al. 2015, *A&A*, 577, A130
- Ferrigno, C., Bozzo, E., & Romano, P. 2020, *A&A*, 642, A73
- Ferrigno, C., Bozzo, E., Sanna, A., et al. 2019, *A&A*, 624, A142
- Forman, W., Jones, C., Cominsky, L., et al. 1978, *ApJS*, 38, 357
- Fritz, S., Kreykenbohm, I., Wilms, J., et al. 2006, *A&A*, 458, 885
- Fürst, F., Pottschmidt, K., Kreykenbohm, I., et al. 2012, *A&A*, 547, A2
- Gehrels, N., Chincarini, G., Giommi, P., et al. 2004, *ApJ*, 611, 1005
- Giacconi, R., Murray, S., Gursky, H., et al. 1972, *ApJ*, 178, 281
- Giménez-García, A., Shenar, T., Torrejón, J. M., et al. 2016, *A&A*, 591, A26
- Giménez-García, A., Torrejón, J. M., Eikmann, W., et al. 2015, *A&A*, 576, A108
- González-Galán, A. 2015, arXiv e-prints, arXiv:1503.01087
- Grinberg, V., Hell, N., El Mellah, I., et al. 2017, *A&A*, 608, A143
- Hannikainen, D. C., Rodriguez, J., Cabanac, C., et al. 2004, *A&A*, 423, L17
- Hemphill, P. B., Rothschild, R. E., Caballero, I., et al. 2013, *ApJ*, 777, 61
- Hubrig, S., Sidoli, L., Postnov, K., et al. 2018, *MNRAS*, 474, L27
- in 't Zand, J. J. M., Baykal, A., & Strohmayer, T. E. 1998, *ApJ*, 496, 386
- in 't Zand, J. J. M., Strohmayer, T. E., & Baykal, A. 1997, *ApJ*, 479, L47
- Inam, S. Ç., Şahiner, Ş., & Baykal, A. 2009, *MNRAS*, 395, 1015
- Islam, N., Maitra, C., Pradhan, P., & Paul, B. 2015, *MNRAS*, 446, 4148
- Jansen, F., Lumb, D., Altieri, B., et al. 2001, *A&A*, 365, L1
- Kaastra, J. S. & Bleeker, J. A. M. 2016, *A&A*, 587, A151
- Kabiraj, S., Islam, N., & Paul, B. 2020, *MNRAS*, 491, 1491
- Kostka, M. & Leahy, D. A. 2010, *MNRAS*, 407, 1182
- Kretschmar, P., Martínez-Núñez, S., Fürst, F., et al. 2019, *Mem. Soc. Astron. Italiana*, 90, 221
- Krimm, H. A., Barthelmy, S. D., Baumgartner, W., et al. 2012, *The Astronomer's Telegram*, 3964, 1
- Krimm, H. A., Holland, S. T., Corbet, R. H. D., et al. 2013, *ApJS*, 209, 14
- Krivonos, R., Tsygankov, S., Lutovinov, A., et al. 2012, *A&A*, 545, A27
- Leahy, D. A. 1991, *MNRAS*, 250, 310
- Leahy, D. A. & Kostka, M. 2008, *MNRAS*, 384, 747
- Makishima, K., Kawai, N., Koyama, K., et al. 1984, *PASJ*, 36, 679
- Manousakis, A. & Walter, R. 2011, *A&A*, 526, A62
- Marshall, N. & Ricketts, M. J. 1980, *MNRAS*, 193, 7P
- Martínez-Núñez, S., Kretschmar, P., Bozzo, E., et al. 2017, *Space Sci. Rev.*, 212, 59
- Masetti, N., Ferreira, T. S., Saito, R. K., Kammers, R., & Minniti, D. 2018, *The Astronomer's Telegram*, 11992, 1
- McCollum, B., Laine, S., & McCollum, M. 2018, *Research Notes of the American Astronomical Society*, 2, 193
- Meidinger, N., Eder, J., Fürmetz, M., et al. 2015, in *Society of Photo-Optical Instrumentation Engineers (SPIE) Conference Series*, Vol. 9601, *UV, X-Ray, and Gamma-Ray Space Instrumentation for Astronomy XIX*, ed. O. H. Siegmund, 96010H
- Mukerjee, K., Agrawal, P. C., Paul, B., et al. 2001a, *ApJ*, 548, 368
- Mukerjee, K., Agrawal, P. C., Paul, B., et al. 2001b, *ApJ*, 548, 368
- Neronov, A., Savchenko, V., Tramacere, A., et al. 2021, *A&A*, 651, A97
- Nespoli, E., Fabregat, J., & Mennickent, R. E. 2008, *A&A*, 486, 911
- Parmar, A. N., White, N. E., Stella, L., Izzo, C., & Ferri, P. 1989, *ApJ*, 338, 359
- Pradhan, P., Bozzo, E., & Paul, B. 2018, *A&A*, 610, A50
- Prat, L., Rodriguez, J., Hannikainen, D. C., & Shaw, S. E. 2008, *MNRAS*, 389, 301
- Puls, J., Vink, J. S., & Najarro, F. 2008, *A&A Rev.*, 16, 209
- Ray, P. S., Arzoumanian, Z., Ballantyne, D., et al. 2019, arXiv e-prints, arXiv:1903.03035
- Rivers, E., Markowitz, A., Pottschmidt, K., et al. 2010, *ApJ*, 709, 179
- Roberts, M. S. E., Michelson, P. F., Leahy, D. A., et al. 2001, *ApJ*, 555, 967
- Rodriguez, J., Garau, A. D., Grebenev, S., et al. 2004, *The Astronomer's Telegram*, 340
- Romano, P., Bozzo, E., Mangano, V., et al. 2015, *A&A*, 576, L4
- Romano, P., Mereghetti, S., Sidoli, L., & Evans, P. A. 2008, *The Astronomer's Telegram*, 1875, 1
- Romano, P., Sidoli, L., Cusumano, G., et al. 2009, *ApJ*, 696, 2068
- Scargle, J. D., Norris, J. P., Jackson, B., & Chiang, J. 2013, *ApJ*, 764, 167
- Sguera, V., Bazzano, A., Bird, A. J., et al. 2006, *ApJ*, 646, 452
- Shakura, N., Postnov, K., Kochetkova, A., & Hjalmarsdotter, L. 2012, *MNRAS*, 420, 216
- Sidoli, L., Esposito, P., Motta, S. E., Israel, G. L., & Rodríguez Castillo, G. A. 2016, *MNRAS*, 460, 3637
- Sidoli, L., Postnov, K., Tiengo, A., et al. 2020, *A&A*, 638, A71
- Sidoli, L., Tiengo, A., Paizis, A., et al. 2017, *ApJ*, 838, 133
- Sugizaki, M., Mitsuda, K., Kaneda, H., et al. 2001, *ApJS*, 134, 77
- Torrejón, J. M., Schulz, N. S., Nowak, M. A., & Kallman, T. R. 2010, *ApJ*, 715, 947
- van Kerkwijk, M. H., van Oijen, J. G. J., & van den Heuvel, E. P. J. 1989, *A&A*, 209, 173
- Varun, Pradhan, P., Maitra, C., Raichur, H., & Paul, B. 2019, *ApJ*, 880, 61
- Verner, D. A., Ferland, G. J., Korista, K. T., & Yakovlev, D. G. 1996, *ApJ*, 465, 487
- Walter, R., Lutovinov, A. A., Bozzo, E., & Tsygankov, S. S. 2015, *A&A Rev.*, 23, 2
- Walter, R. & Zurita Heras, J. 2007, *A&A*, 476, 335
- Watanabe, K., Bozzo, E., Mereghetti, S., & Gotz, C. B. D. 2010, *The Astronomer's Telegram*, 2482, 1
- Watanabe, S., Sako, M., Ishida, M., et al. 2006, *ApJ*, 651, 421
- Wen, L., Levine, A. M., Corbet, R. H. D., & Bradt, H. V. 2006, *ApJS*, 163, 372
- Wilms, J., Allen, A., & McCray, R. 2000, *ApJ*, 542, 914
- Zhang, S. N., Feroci, M., Santangelo, A., et al. 2016, in *Society of Photo-Optical Instrumentation Engineers (SPIE) Conference Series*, Vol. 9905, *Space Telescopes and Instrumentation 2016: Ultraviolet to Gamma Ray*, ed. J.-W. A. den Herder, T. Takahashi, & M. Bautz, 99051Q

Appendix A: Refinement of the IGR J19140+0951 orbital period.

To refine the early determination of the source ephemerides by Corbet et al. (2004), we first downloaded the full ASM light curve from the online archive (from MJD 50088 to 55846) at the maximum available timing resolution. We computed the Lomb-Scargle periodogram (Scargle et al. 2013) with an oversampling factor of four and limiting ourselves to 0.4 times the average Nyquist frequency. Following Corbet et al. (2007), we weighted each bin of the light curve with $(f\sigma + V_S)^{-1}$ and $f = 1.2$. By fitting the peak with a Sync curve we determined a period of 13.5550 ± 0.0005 d.

The source is also monitored by *Swift*/BAT and the up-to-date light curve in the 15–50 keV energy band (time resolution of 1 satellite orbit) can be downloaded from the *Swift*/BAT Hard X-ray Transient Monitor on-line page (Krimm et al. 2013)⁵. The arrival time of the collected photons was converted to the solar system barycenter frame using the *earth2sun* program. We excluded data from 2019, as we found that the orbital periodicity is not significant in the corresponding data. We then computed the Lomb-Scargle periodogram with a weight of σ^{-1} as in D’Ài et al. (2011); the fit to the peak yields an orbital period of 13.55273 ± 0.00005 d in the time range MJD 53416–59597. The periods from ASM and *Swift*/BAT differ by almost five equivalent Gaussian sigma, while the improvement of the uncertainty is linked to the higher signal of the source in *Swift*/BAT combined with the slightly longer baseline. To look for a possible decrease of the orbital period, we sliced the *Swift*/BAT lightcurve in several intervals with duration ranging from four months to three years, but no significant trend was detectable. Therefore, we conclude that the different orbital periods from ASM and *Swift*/BAT is most probably spurious and linked to the different data quality.

In Fig. A.1, we show the orbital profile as measured from the BAT data in the 15–50 keV band using our refined orbital period estimate.

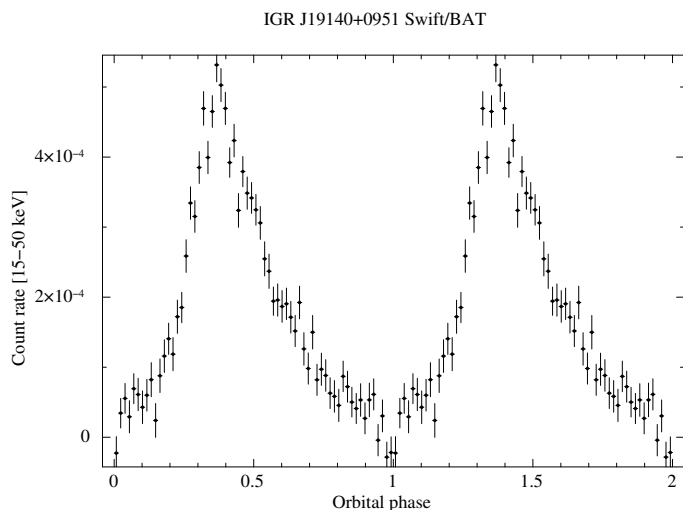


Fig. A.1: IGR J19140+0951 orbital profile obtained from the *Swift*/BAT light curve (15–50 keV energy range) folded at the newly refined period of 13.55273 d over 64 bins. The assumed reference time is MJD 52061.42 and data span from 15 Feb 2005 to 18 Jan 2022. The profile is displayed twice for clarity.

Table B.1: *Swift*/XRT observation log for IGR J17315+3221.

Sequence	MJD	Start time (UT)	End time (UT)	Exp. (s)
00034659002	57608.31510	2016-08-08 07:33:36	2016-08-08 07:52:54	1148
00034659003	57610.44377	2016-08-10 10:39:01	2016-08-10 18:59:52	1610
00034659004	57611.37894	2016-08-11 09:05:40	2016-08-11 09:21:53	973
00034659005	57612.17438	2016-08-12 04:11:06	2016-08-12 04:28:54	1068
00034659006	57615.42504	2016-08-15 10:12:03	2016-08-15 10:29:54	1071
00034659007	57616.22967	2016-08-16 05:30:43	2016-08-16 05:46:54	970
00034659009	57618.08242	2016-08-18 01:58:40	2016-08-18 02:15:53	1033
00034659010	57619.47689	2016-08-19 11:26:42	2016-08-19 11:44:53	1091
00034659011	57620.47378	2016-08-20 11:22:14	2016-08-20 11:39:55	1061
00043517001	56171.76098	2012-09-01 18:15:48	2012-09-01 18:19:56	248
00043517002	56173.31138	2012-09-03 07:28:23	2012-09-03 07:32:56	273
00043517003	56177.38995	2012-09-07 09:21:31	2012-09-07 09:29:55	504
00043524001	56172.23429	2012-09-02 05:37:22	2012-09-02 05:46:54	572
00043524002	56178.26009	2012-09-08 06:14:31	2012-09-08 06:22:55	504

Notes. We report the observing sequence and date (MJD of the middle of the observation), start and end times (UT), and XRT exposure time (Exp.). Note that that start and stop time of each observation is given in the format yyyy-mm-dd hh:mm:ss.

Appendix B: IGR J17315–3221

IGR J17315–3221 was reported for the first time in the catalogue of the *INTEGRAL* sources published by Krivonos et al. (2012) and suspected to be another HMXB discovered by *INTEGRAL*, possibly an SgXB (see also Clavel et al. 2019). The source is reported in the catalogue at a best determined position of RA=262.818, DEC=−32.306, with an associated positional accuracy of 2 arcmin. The estimated average flux in the 17–60 keV energy band was 4×10^{-12} erg cm² s^{−1}. We show here that the reported discovery of this source is most likely to result from an artifact of the *INTEGRAL* data analysis and a re-analysis of all available *INTEGRAL* data show no evidence of a significant source detection at a position consistent with that reported previously for IGR J17315–3221.

As IGR J17315–3221 was initially announced to be a likely additional HMXB discovered by *INTEGRAL*, this source was included among the monitored targets in our observational campaigns carried out with *Swift*. XRT performed observations in the direction of the source between 2012 and 2016, summing up to a total available exposure time of 12.1 ks (see Table C.5, where the target ID 34659 identifies our 10, 1 ks pointed observations, the remainder being archival ones). We extracted first an image of the XRT field of view (FoV) for each observation and then a single image stacking all data together in the 0.3–10 keV energy band. No X-ray source is detected within 2 arcmin from the best reported position of IGR J17315–3221 in the single images or in the stacked image obtained with all available data. A 3σ upper limit in the 0.3–10 keV was calculated by using *sosta* within the XIMAGE task and a circular background region (radius of 56 pixels) away from field sources, at 1.7×10^{-3} cts s^{−1}; by using PIMMS (v4.11b), when assuming a photon index of 2.1 and an absorbing column of 1.23×10^{22} cm^{−2}, we obtain an observed (unabsorbed) flux of 9.9×10^{-14} (2.30×10^{-13} erg cm² s^{−1}).

Motivated by the lack of any soft X-ray counterpart in the XRT data, we re-analyzed all *INTEGRAL* archival data available around the position of IGR J17315–3221. Using the latest available calibration and software version (Offline Scientific Analysis 11.2) from the multimessenger online analysis platform⁶, we extracted a mosaic image in the 20–60 keV energy band using first

⁵ <https://swift.gsfc.nasa.gov/results/transients/>

⁶ <https://www.astro.unige.ch/mmoda/>

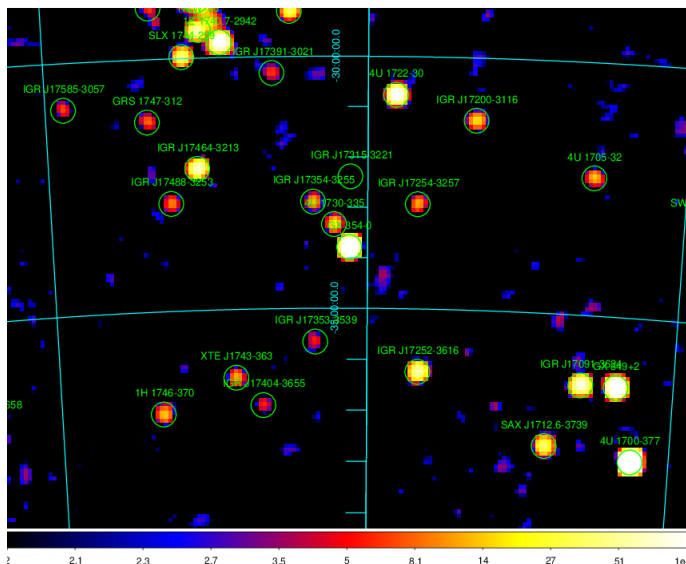


Fig. B.1: *INTEGRAL* IBIS/ISGRI significance map in the 20–60 keV energy range of the region around IGR J17315–3221 obtained from all available pointings at less than twelve degrees from the source collected in the time period 2004–2012. No significant detection of the previously reported source could be found.

the same IBIS/ISGRI data considered by Krivonos et al. (2012) and then from 2014 to 2021 (restricting the pointings to a maximum allowed off-axis angle of 12° to avoid large instrument systematics⁷). Neither of the two images shows a significant detection of any source at a location compatible with the reported position of IGR J17315–3221. From January 2004 to December 2012, we obtained a 3σ upper limit on the source flux in the 20–60 keV energy band of 0.4 mCrab (5×10^{-12} erg s $^{-1}$ cm $^{-2}$) in 4.2 Ms of effective exposure on the source. From January 2013 to October 2021, we obtained a slightly worse upper limit of 0.6 mCrab (7×10^{-12} erg s $^{-1}$ cm $^{-2}$) in 3.7 Ms, owing to the degraded instrument response at low energy during the mission lifetime. To obtain these upper limits, we have elaborated the original mosaics using *SExtractor* (Bertin & Arnouts 1996) in its most recent implementation (version 2.25.2)⁸. This is done to correct for the coding noise that is particularly pronounced in the Galactic center region, due to the large number of bright sources and diffuse emission. We apply the software with a box size of four pixels and a detection threshold for sources of three. We show the cleaned significance map for the period 2004–2012 in Fig. B.1 (the map in the following period is similar).

From this re-analysis of *INTEGRAL* data and the *Swift*/XRT non-detection, we conclude that IGR J17315–3221 is not a real astrophysical source, but rather an analysis artifact.

Appendix C: *Swift* data log tables

In the following tables, we show the logs of the *Swift*/XRT observations for each source included in the paper.

In Tables C.1–C.3, the columns represent: observing sequence, observation date (mid-observation MJD), orbital phase, start and end times of the observations (UT), exposure time in seconds,

⁷ See details in the IBIS/ISGRI data analysis manual at <https://www.isdc.unige.ch/integral/analysis>.

⁸ The documentation is available at the URL <https://sextractor.readthedocs.io/en/latest/index.html>.

and the 0.3–10 keV flux in units of 10^{-11} erg cm $^{-2}$ s $^{-1}$; missing values are due to insufficient counts to perform any spectral analysis.

In the case of XTE J1855–026 (Table C.4), also the log of the BAT data are reported.

Note that in these tables uncertainties are at 90% confidence level.

Table C.1: *Swift*/XRT observation log for 4U J1907+097.

Sequence	MJD	Phase	Start time (UT) (yyyy-mm-dd hh:mm:ss)	End time (UT) (yyyy-mm-dd hh:mm:ss)	Exposure (s)	Flux
00033483001	57069.19720	0.96	2015-02-16 04:36:01	2015-02-16 04:51:54	953	13.3 ^{+2.4} _{-2.0}
00033483003	57076.77906	0.87	2015-02-23 18:34:47	2015-02-23 18:48:54	847	28.3 ^{+7.7} _{-6.2}
00033483004	57079.45028	0.19	2015-02-26 10:39:53	2015-02-26 10:56:54	1020	14.6 ^{+2.2} _{-1.9}
00033483005	57083.24917	0.64	2015-03-02 05:49:41	2015-03-02 06:07:54	1093	69.8 ^{+7.8} _{-7.0}
00033483006	57086.50529	0.03	2015-03-05 11:59:17	2015-03-05 12:15:55	998	9.5 ^{+2.1} _{-1.7}
00033483007	57090.35591	0.49	2015-03-09 08:24:05	2015-03-09 08:40:55	1010	2.8 ^{+0.7} _{-0.5}
00033483008	57093.95062	0.92	2015-03-12 22:40:50	2015-03-12 22:56:55	965	17.2 ^{+4.1} _{-3.3}
00033483009	57097.34327	0.32	2015-03-16 08:06:41	2015-03-16 08:21:56	915	21.3 ^{+3.0} _{-2.6}
00033483010	57100.28330	0.67	2015-03-19 06:39:57	2015-03-19 06:55:55	958	27.2 ^{+3.9} _{-3.3}
00033483011	57104.94361	0.23	2015-03-23 22:30:39	2015-03-23 22:46:56	978	19.0 ^{+2.7} _{-2.3}
00033483012	57107.87126	0.58	2015-03-26 20:46:19	2015-03-26 21:02:54	995	63.9 ^{+7.6} _{-6.8}
00033483014	57114.66061	0.39	2015-04-02 15:43:43	2015-04-02 15:58:50	908	41.9 ^{+5.8} _{-5.0}
00033483015	57118.05140	0.80	2015-04-06 01:05:06	2015-04-06 01:22:54	1068	17.4 ^{+3.6} _{-3.0}
00033483016	57121.11656	0.16	2015-04-09 02:39:45	2015-04-09 02:55:56	970	1.5 ^{+0.4} _{-0.3}
00033483017	57125.11082	0.64	2015-04-12 07:28:14	2015-04-13 21:50:54	1336	35.9 ^{+3.8} _{-3.4}
00033483018	57128.81887	0.08	2015-04-16 19:30:25	2015-04-16 19:47:55	1051	40.6 ^{+4.2} _{-3.8}
00033483019	57132.02167	0.46	2015-04-20 00:22:30	2015-04-20 00:39:56	1043	6.8 ^{+1.3} _{-1.1}
00033483020	57135.02061	0.82	2015-04-23 00:21:26	2015-04-23 00:37:54	988	1.1 ^{+0.4} _{-0.3}
00033483021	57139.20940	0.32	2015-04-27 04:53:09	2015-04-27 05:09:54	1005	0.6 ^{+0.4} _{-0.3}
00033483022	57142.33898	0.70	2015-04-30 07:59:21	2015-04-30 08:16:54	1053	63.2 ^{+8.9} _{-7.8}
00033483023	57146.33073	0.17	2015-05-04 07:47:35	2015-05-04 08:04:55	1041	36.1 ^{+4.6} _{-4.1}
00033483024	57149.25551	0.52	2015-05-07 05:55:57	2015-05-07 06:19:54	1437	49.1 ^{+5.3} _{-4.8}
00033483025	57153.17402	0.99	2015-05-11 04:10:32	2015-05-11 04:30:55	5	–
00033483026	57156.70637	0.41	2015-05-14 16:49:25	2015-05-14 17:04:55	930	0.5 ^{+0.3} _{-0.2}
00033483027	57160.75299	0.89	2015-05-18 17:56:41	2015-05-18 18:11:56	915	14.5 ^{+2.6} _{-2.1}
00033483028	57163.65917	0.24	2015-05-21 14:59:29	2015-05-21 16:38:54	908	13.4 ^{+1.8} _{-1.6}
00033483029	57167.87186	0.74	2015-05-25 20:50:01	2015-05-25 21:00:55	654	22.8 ^{+4.6} _{-3.8}
00033483030	57170.07622	0.01	2015-05-28 01:44:37	2015-05-28 01:54:56	617	26.4 ^{+5.1} _{-4.2}
00033483031	57174.06796	0.48	2015-06-01 01:29:49	2015-06-01 01:45:54	965	12.5 ^{+2.4} _{-2.0}
00033483033	57181.70856	0.40	2015-06-08 16:47:44	2015-06-08 17:12:54	1509	91.4 ^{+8.8} _{-8.0}
00033483034	57184.38300	0.72	2015-06-11 07:32:07	2015-06-11 10:50:54	1056	42.1 ^{+4.3} _{-3.9}
00033483035	57188.64007	0.22	2015-06-15 15:14:28	2015-06-15 15:28:55	868	2.9 ^{+0.7} _{-0.5}
00033483036	57191.42814	0.56	2015-06-18 10:08:07	2015-06-18 10:24:55	1008	32.6 ^{+3.8} _{-3.4}
00033483037	57195.15266	0.00	2015-06-22 03:31:44	2015-06-22 03:47:54	970	42.2 ^{+5.2} _{-4.7}
00033483038	57198.68399	0.42	2015-06-25 16:16:57	2015-06-25 16:32:55	958	20.0 ^{+3.3} _{-2.8}
00033483039	57202.91001	0.93	2015-06-29 20:59:52	2015-06-29 22:40:57	955	25.5 ^{+3.8} _{-3.3}
00033483040	57205.11780	0.19	2015-07-02 02:42:20	2015-07-02 02:56:55	875	20.2 ^{+3.0} _{-2.6}
00033483041	57209.84092	0.76	2015-07-06 20:02:54	2015-07-06 20:18:55	960	33.0 ^{+5.4} _{-4.6}
00033483042	57212.30136	0.05	2015-07-09 07:08:01	2015-07-09 07:19:53	712	42.1 ^{+5.0} _{-4.4}
00033483043	57216.97833	0.61	2015-07-13 23:24:41	2015-07-13 23:32:53	491	50.1 ^{+8.7} _{-7.2}
00033483044	57219.17442	0.87	2015-07-16 04:08:27	2015-07-16 04:13:53	326	16.9 ^{+4.9} _{-3.7}
00033483045	57223.31399	0.36	2015-07-20 04:56:23	2015-07-20 10:07:54	762	12.0 ^{+2.3} _{-2.0}
00033483046	57226.51238	0.75	2015-07-23 06:55:46	2015-07-23 17:39:52	933	38.2 ^{+4.4} _{-3.9}
00033483047	57230.33604	0.20	2015-07-27 07:55:52	2015-07-27 08:11:55	963	17.7 ^{+3.2} _{-2.7}
00033483048	57233.28949	0.56	2015-07-30 02:46:48	2015-07-30 11:06:55	905	21.8 ^{+3.4} _{-2.9}
00033483049	57237.31020	0.04	2015-08-03 07:19:28	2015-08-03 07:33:53	865	11.8 ^{+2.1} _{-1.7}
00033483050	57240.04352	0.36	2015-08-06 00:54:24	2015-08-06 01:10:55	990	10.6 ^{+2.9} _{-2.2}
00033483051	57244.70114	0.92	2015-08-10 16:41:22	2015-08-10 16:57:54	993	5.3 ^{+1.2} _{-0.9}
00033483052	57247.73589	0.28	2015-08-13 12:08:28	2015-08-13 23:10:53	888	17.9 ^{+2.5} _{-2.2}

Table C.1: continued.

Sequence	MJD	Phase	Start time (UT)	End time (UT)	Exposure	Flux
00033483053	57251.75651	0.76	2015-08-17 18:00:50	2015-08-17 18:17:53	1023	32.7 ^{+4.6} _{-4.0}
00033483054	57254.88463	0.13	2015-08-20 21:05:50	2015-08-20 21:21:53	963	24.8 ^{+3.0} _{-2.7}
00033483055	57258.20110	0.53	2015-08-24 04:41:15	2015-08-24 04:57:53	998	56.0 ^{+7.6} _{-6.6}
00033483056	57261.38728	0.91	2015-08-27 09:08:27	2015-08-27 09:26:53	1106	20.8 ^{+4.1} _{-3.3}
00033483057	57265.72559	0.43	2015-08-31 17:16:46	2015-08-31 17:32:56	970	36.5 ^{+4.2} _{-3.8}
00033483058	57268.24792	0.73	2015-09-03 04:16:07	2015-09-03 07:37:53	978	25.7 ^{+4.0} _{-3.4}
00033483059	57273.62788	0.37	2015-09-08 13:15:21	2015-09-08 16:52:55	1156	4.1 ^{+0.9} _{-0.7}
00033483060	57275.08861	0.55	2015-09-10 01:59:16	2015-09-10 02:15:54	998	–
00033483061	57279.21154	0.04	2015-09-14 04:56:19	2015-09-14 05:12:55	995	3.8 ^{+0.7} _{-0.6}
00033483062	57282.26433	0.40	2015-09-17 06:20:29	2015-09-17 06:20:46	18	–
00033483063	57286.87282	0.95	2015-09-21 20:48:49	2015-09-21 21:04:54	965	41.8 ^{+5.6} _{-4.9}
00033483064	57289.39770	0.25	2015-09-24 09:23:28	2015-09-24 09:41:54	1106	30.2 ^{+4.2} _{-3.7}
00033483065	57293.24991	0.71	2015-09-28 05:50:49	2015-09-28 06:08:55	1086	33.7 ^{+4.2} _{-3.8}

Table C.2: *Swift*/XRT observation log for IGR J19140+0951.

Sequence	MJD	Phase	Start time (UT) (yyyy-mm-dd hh:mm:ss)	End time (UT) (yyyy-mm-dd hh:mm:ss)	Exposure (s)	Flux
00030393003	57071.13152	0.65	2015-02-18 03:00:51	2015-02-18 03:17:54	1023	3.1 ^{+0.9} _{-0.7}
00030393004	57074.05215	0.86	2015-02-21 01:06:15	2015-02-21 01:23:56	1061	0.7 ^{+0.6} _{-0.3}
00030393005	57078.11378	0.16	2015-02-25 02:35:45	2015-02-25 02:51:55	970	0.3 ^{+0.2} _{-0.1}
00030393006	57081.17754	0.39	2015-02-28 04:07:22	2015-02-28 04:23:55	993	11.4 ^{+2.0} _{-1.7}
00030393007	57085.50884	0.71	2015-03-04 12:04:32	2015-03-04 12:20:55	983	4.9 ^{+1.7} _{-1.2}
00030393008	57088.50679	0.93	2015-03-07 12:01:37	2015-03-07 12:17:55	925	0.6 ^{+0.8} _{-0.3}
00030393009	57092.50049	0.22	2015-03-11 11:51:30	2015-03-11 12:09:53	1103	4.3 ^{+1.2} _{-0.9}
00030393010	57095.29009	0.43	2015-03-14 06:49:31	2015-03-14 07:05:56	985	4.4 ^{+1.2} _{-0.9}
00030393011	57099.67249	0.75	2015-03-18 15:59:50	2015-03-18 16:16:56	1025	4.7 ^{+1.0} _{-0.8}
00030393012	57102.74830	0.98	2015-03-21 17:49:24	2015-03-21 18:05:54	978	–
00030393013	57106.13932	0.23	2015-03-25 03:12:37	2015-03-25 03:28:54	960	7.9 ^{+1.6} _{-1.4}
00030393014	57109.73308	0.50	2015-03-28 17:27:19	2015-03-28 17:43:57	998	10.0 ^{+2.0} _{-1.6}
00030393015	57113.91388	0.80	2015-04-01 21:47:02	2015-04-01 22:04:55	1073	–
00030393016	57116.84270	0.02	2015-04-04 20:05:02	2015-04-04 20:21:55	1013	4.7 ^{+0.9} _{-0.8}
00030393017	57120.50776	0.29	2015-04-08 12:00:26	2015-04-08 12:21:54	1158	23.0 ^{+3.9} _{-3.3}
00030393018	57123.03947	0.48	2015-04-11 00:48:43	2015-04-11 01:04:56	973	3.2 ^{+1.1} _{-0.8}
00030393019	57127.82063	0.83	2015-04-15 19:32:31	2015-04-15 19:50:54	1103	9.9 ^{+1.5} _{-1.3}
00030393020	57130.02916	0.99	2015-04-18 00:39:02	2015-04-18 00:44:56	354	7.8 ^{+3.1} _{-2.1}
00030393021	57134.08242	0.29	2015-04-22 01:50:27	2015-04-22 02:06:54	988	19.7 ^{+5.3} _{-4.1}
00030393022	57137.54770	0.55	2015-04-25 13:00:27	2015-04-25 13:16:55	988	5.3 ^{+1.2} _{-0.9}
00030393023	57141.53064	0.84	2015-04-29 12:35:19	2015-04-29 12:52:55	1056	6.0 ^{+1.3} _{-1.0}
00030393024	57144.12763	0.03	2015-05-02 02:55:41	2015-05-02 03:11:54	973	–
00030393025	57148.05961	0.32	2015-05-06 01:17:45	2015-05-06 01:33:55	970	7.7 ^{+2.1} _{-1.6}
00030393026	57151.78003	0.60	2015-05-09 16:53:34	2015-05-09 20:32:54	1364	7.9 ^{+1.4} _{-1.2}
00030393027	57155.04283	0.84	2015-05-13 00:53:26	2015-05-13 01:09:54	988	0.4 ^{+0.5} _{-0.2}
00030393028	57158.82522	0.12	2015-05-16 19:44:42	2015-05-16 19:51:55	434	–
00030393029	57162.89551	0.42	2015-05-20 21:28:09	2015-05-20 21:30:54	165	–
00030393030	57165.87459	0.64	2015-05-23 20:51:53	2015-05-23 21:06:55	903	2.9 ^{+1.1} _{-0.8}
00030393031	57169.87156	0.93	2015-05-27 20:48:10	2015-05-27 21:01:55	825	–
00030393033	57176.66578	0.43	2015-06-03 15:48:33	2015-06-03 16:08:54	1221	1.5 ^{+0.7} _{-0.4}
00030393034	57179.78132	0.66	2015-06-06 18:36:16	2015-06-06 18:53:54	1058	4.1 ^{+1.0} _{-0.8}
00030393035	57183.21927	0.92	2015-06-10 04:21:34	2015-06-10 06:09:55	722	0.7 ^{+0.7} _{-0.3}
00030393036	57186.50262	0.16	2015-06-13 11:54:38	2015-06-13 12:12:54	1096	0.9 ^{+0.6} _{-0.3}

Table C.2: continued.

Sequence	MJD	Phase	Start time (UT)	End time (UT)	Exposure	Flux
00030393037	57190.17122	0.43	2015-06-17 03:59:12	2015-06-17 04:13:54	883	–
00030393038	57193.93137	0.71	2015-06-20 21:31:26	2015-06-20 23:10:54	1108	0.03 ^{+0.03} _{–0.02}
00030393039	57197.54561	0.97	2015-06-24 12:55:27	2015-06-24 13:15:54	1226	17.6 ^{+3.2} _{–2.7}
00030393040	57200.63216	0.20	2015-06-27 14:24:41	2015-06-27 15:55:54	1294	5.6 ^{+1.4} _{–1.1}
00030393041	57204.52040	0.49	2015-07-01 12:20:50	2015-07-01 12:37:53	1003	3.0 ^{+1.0} _{–0.7}
00030393042	57207.51383	0.71	2015-07-04 12:10:56	2015-07-04 12:28:54	1078	5.8 ^{+1.2} _{–1.0}
00030393043	57211.71016	0.02	2015-07-08 16:54:20	2015-07-08 17:10:55	995	1.3 ^{+1.2} _{–0.8}
00030393044	57214.07191	0.19	2015-07-11 01:08:13	2015-07-11 02:18:52	918	2.7 ^{+0.9} _{–0.7}
00030393045	57218.44256	0.52	2015-07-15 10:35:40	2015-07-15 10:38:54	193	–
00030393046	57221.76517	0.76	2015-07-18 18:14:48	2015-07-18 18:28:53	845	0.5 ^{+0.3} _{–0.2}
00030393047	57225.28945	0.02	2015-07-22 06:48:41	2015-07-22 07:04:54	973	2.8 ^{+0.7} _{–0.6}
00030393048	57228.40191	0.25	2015-07-25 09:31:04	2015-07-25 09:46:27	920	28.4 ^{+5.2} _{–4.3}
00030393049	57232.40124	0.55	2015-07-29 09:29:40	2015-07-29 09:45:53	973	6.0 ^{+1.6} _{–1.2}
00030393050	57235.62146	0.78	2015-08-01 10:37:54	2015-08-01 19:11:53	1038	–
00030393051	57239.04772	0.04	2015-08-05 01:03:30	2015-08-05 01:13:55	624	–
00030393052	57242.03565	0.26	2015-08-08 00:42:47	2015-08-08 00:59:53	1025	27.1 ^{+6.3} _{–5.1}
00030393053	57246.23508	0.57	2015-08-12 05:30:08	2015-08-12 05:46:53	1005	1.8 ^{+0.9} _{–0.6}
00030393054	57249.03230	0.77	2015-08-15 00:38:08	2015-08-15 00:54:53	1005	0.9 ^{+0.4} _{–0.3}
00030393055	57253.55333	0.11	2015-08-19 13:05:40	2015-08-19 13:27:54	1334	1.5 ^{+0.5} _{–0.4}
00030393056	57256.47959	0.32	2015-08-22 11:21:20	2015-08-22 11:39:53	1113	4.1 ^{+0.9} _{–0.7}
00030393057	57260.33788	0.61	2015-08-26 07:58:11	2015-08-26 08:14:54	1003	0.8 ^{+0.4} _{–0.2}
00030393058	57263.36187	0.83	2015-08-29 07:53:17	2015-08-29 09:28:53	968	2.0 ^{+0.7} _{–0.5}
00030393059	57267.31970	0.12	2015-09-02 07:30:49	2015-09-02 07:49:55	1146	1.5 ^{+0.9} _{–0.6}
00030393061	57274.10016	0.62	2015-09-09 02:08:32	2015-09-09 02:39:54	1063	4.9 ^{+1.1} _{–0.9}
00030393062	57277.89862	0.90	2015-09-12 21:30:08	2015-09-12 21:37:54	466	3.3 ^{+1.2} _{–0.9}
00030393063	57281.68750	0.18	2015-09-16 16:22:04	2015-09-16 16:37:55	950	0.9 ^{+0.4} _{–0.3}
00030393064	57284.27302	0.37	2015-09-19 06:14:24	2015-09-19 06:51:53	1033	5.9 ^{+1.8} _{–1.3}
00030393065	57288.07229	0.65	2015-09-23 00:03:16	2015-09-23 03:24:55	797	7.8 ^{+1.5} _{–1.2}
00030393066	57291.92352	0.94	2015-09-26 22:01:49	2015-09-26 22:17:54	965	1.6 ^{+0.6} _{–0.4}
00030393067	57295.78035	0.22	2015-09-30 18:35:30	2015-09-30 18:51:53	983	3.9 ^{+1.0} _{–0.7}

Table C.3: *Swift*/XRT observation log for IGR J16393–4643.

Sequence	MJD	Phase	Start time (UT)	End time (UT)	Exposure	Flux
			(yyyy-mm-dd hh:mm:ss)	(yyyy-mm-dd hh:mm:ss)	(s)	
00034135001	57408.33228	0.49	2016-01-21 07:50:05	2016-01-21 08:06:53	1008	1.9 ^{+0.7} _{–0.5}
00034135002	57409.06321	0.66	2016-01-22 01:23:07	2016-01-22 01:38:55	948	0.6 ^{+0.9} _{–0.3}
00034135003	57410.47124	0.99	2016-01-23 11:10:17	2016-01-23 11:26:53	995	–
00034135004	57411.19096	0.16	2016-01-24 04:26:05	2016-01-24 04:43:53	1068	2.4 ^{+0.8} _{–0.6}
00034135005	57412.31988	0.43	2016-01-25 07:32:22	2016-01-25 07:48:53	990	4.6 ^{+1.1} _{–0.9}
00034135006	57413.31668	0.67	2016-01-26 07:28:08	2016-01-26 07:43:53	945	2.8 ^{+1.0} _{–0.8}
00034135008	57415.38120	0.15	2016-01-28 08:59:56	2016-01-28 09:17:55	1078	2.3 ^{+1.1} _{–0.7}
00034135009	57416.10815	0.32	2016-01-29 02:27:54	2016-01-29 02:43:34	940	4.8 ^{+1.2} _{–1.0}
00034135010	57417.24288	0.59	2016-01-30 05:41:35	2016-01-30 05:57:55	980	3.0 ^{+0.9} _{–0.7}
00034135011	57418.04097	0.78	2016-01-31 00:51:04	2016-01-31 01:06:54	950	1.9 ^{+0.9} _{–0.6}
00034135012	57419.23200	0.06	2016-02-01 05:25:16	2016-02-01 05:42:54	1058	2.6 ^{+1.1} _{–0.7}
00034135013	57420.83151	0.44	2016-02-02 19:48:49	2016-02-02 20:05:55	1025	3.4 ^{+1.0} _{–0.8}
00034135014	57421.03322	0.49	2016-02-03 00:38:46	2016-02-03 00:56:54	1088	2.9 ^{+0.9} _{–0.7}
00034135015	57422.49361	0.83	2016-02-04 03:47:43	2016-02-04 19:53:53	1785	2.1 ^{+0.8} _{–0.6}
00034135016	57423.22185	0.00	2016-02-05 05:11:01	2016-02-05 05:27:54	1013	7.6 ^{+1.9} _{–1.6}
00034135017	57424.94619	0.41	2016-02-06 22:35:08	2016-02-06 22:49:53	885	3.9 ^{+2.9} _{–1.8}

Table C.3: continued.

Sequence	MJD	Phase	Start time (UT)	End time (UT)	Exposure	Flux
00034135018	57425.67767	0.58	2016-02-07 16:06:46	2016-02-07 16:24:54	1088	2.5 ^{+0.8} _{-0.6}
00034135019	57426.87456	0.86	2016-02-08 20:50:49	2016-02-08 21:07:54	1025	0.1 ^{+0.3} _{-0.1}
00034135020	57427.80319	0.08	2016-02-09 19:09:18	2016-02-09 19:23:53	875	2.2 ^{+1.1} _{-0.7}
00034135021	57428.14085	0.16	2016-02-10 03:14:44	2016-02-10 03:30:54	970	2.7 ^{+0.9} _{-0.7}
00034135022	57429.14492	0.40	2016-02-11 00:16:27	2016-02-11 06:40:54	953	2.9 ^{+0.9} _{-0.7}
00034135023	57430.10943	0.63	2016-02-12 00:03:16	2016-02-12 05:11:53	1339	2.3 ^{+0.6} _{-0.5}
00034135024	57431.37563	0.93	2016-02-13 08:07:54	2016-02-13 09:53:54	1013	–
00034135025	57432.07308	0.09	2016-02-14 01:38:34	2016-02-14 01:51:54	800	3.3 ^{+1.3} _{-0.9}
00034135026	57433.26786	0.37	2016-02-15 06:18:31	2016-02-15 06:32:54	863	–
00034135027	57434.36777	0.63	2016-02-16 01:35:15	2016-02-16 16:03:54	890	2.4 ^{+0.9} _{-0.6}
00034135028	57435.79345	0.97	2016-02-17 18:55:15	2016-02-17 19:09:53	878	3.3 ^{+1.2} _{-0.9}
00034135029	57436.78924	0.20	2016-02-18 18:49:38	2016-02-18 19:03:21	822	2.8 ^{+1.4} _{-0.9}
00034135030	57437.78604	0.44	2016-02-19 18:42:51	2016-02-19 19:00:55	1083	4.5 ^{+1.3} _{-1.0}
00034135031	57438.78265	0.67	2016-02-20 18:38:08	2016-02-20 18:55:54	1066	1.2 ^{+0.5} _{-0.4}
00034135032	57439.77768	0.91	2016-02-21 18:30:49	2016-02-21 18:48:52	1083	1.3 ^{+0.8} _{-0.5}
00034135033	57440.77698	0.14	2016-02-22 18:30:46	2016-02-22 18:46:56	970	4.3 ^{+1.9} _{-1.2}
00034135034	57441.70582	0.36	2016-02-23 16:47:51	2016-02-23 17:04:54	1023	2.7 ^{+0.9} _{-0.7}
00034135035	57442.09999	0.46	2016-02-24 02:15:03	2016-02-24 02:32:54	1071	2.3 ^{+0.7} _{-0.5}
00034135036	57443.68719	0.83	2016-02-25 16:22:12	2016-02-25 16:36:52	880	–
00034135037	57444.41879	0.00	2016-02-26 09:55:11	2016-02-26 10:10:54	943	2.4 ^{+1.0} _{-0.7}
00034135038	57445.23192	0.20	2016-02-27 05:32:02	2016-02-27 05:35:52	231	–
00034135039	57446.35042	0.46	2016-02-28 03:34:19	2016-02-28 13:14:53	1371	2.6 ^{+0.8} _{-0.6}
00034135040	57446.75943	0.56	2016-02-28 03:52:15	2016-02-29 08:34:53	1356	2.9 ^{+0.8} _{-0.6}
00034135041	57448.60692	0.99	2016-03-01 14:26:00	2016-03-01 14:41:55	955	2.7 ^{+1.3} _{-0.8}
00034135042	57449.35112	0.17	2016-03-02 08:19:19	2016-03-02 08:31:54	755	5.9 ^{+1.9} _{-1.4}
00034135044	57451.40197	0.65	2016-03-04 09:30:46	2016-03-04 09:46:54	968	2.8 ^{+1.0} _{-0.7}
00034135045	57452.60000	0.93	2016-03-05 14:15:07	2016-03-05 14:32:52	1066	1.2 ^{+1.0} _{-0.7}
00034135046	57453.73040	0.20	2016-03-06 17:23:37	2016-03-06 17:39:55	978	3.2 ^{+1.5} _{-1.1}
00034135047	57454.26308	0.33	2016-03-07 06:10:46	2016-03-07 06:26:54	968	4.5 ^{+1.4} _{-1.1}
00034135048	57455.49565	0.62	2016-03-08 11:09:33	2016-03-08 12:37:54	953	2.9 ^{+1.0} _{-0.8}
00034135049	57456.12555	0.77	2016-03-09 02:53:41	2016-03-09 03:07:53	852	2.6 ^{+1.2} _{-0.8}
00034135050	57457.12260	0.00	2016-03-10 02:49:10	2016-03-10 03:03:53	883	3.9 ^{+1.4} _{-1.0}
00034135051	57458.39444	0.30	2016-03-11 09:19:05	2016-03-11 09:36:53	1068	1.4 ^{+0.5} _{-0.3}
00034135052	57459.25599	0.51	2016-03-12 06:00:21	2016-03-12 06:16:54	993	3.0 ^{+1.2} _{-0.9}
00034135053	57460.31769	0.76	2016-03-13 07:30:02	2016-03-13 07:44:55	893	2.6 ^{+1.1} _{-0.8}
00034135054	57461.44428	0.02	2016-03-14 10:31:36	2016-03-14 10:47:54	978	1.9 ^{+0.8} _{-0.5}
00034135055	57462.83928	0.35	2016-03-15 20:00:13	2016-03-15 20:16:53	1000	4.3 ^{+1.1} _{-0.9}
00034135056	57463.90409	0.60	2016-03-16 21:33:51	2016-03-16 21:49:54	963	2.1 ^{+0.8} _{-0.5}
00034135057	57464.63881	0.78	2016-03-17 15:11:52	2016-03-17 15:27:53	960	0.6 ^{+0.6} _{-0.3}
00034135058	57465.33851	0.94	2016-03-18 07:27:00	2016-03-18 08:47:54	812	1.8 ^{+0.8} _{-1.1}
00034135059	57466.33907	0.18	2016-03-19 00:52:37	2016-03-19 15:23:53	1041	2.5 ^{+1.1} _{-0.7}
00034135060	57467.16779	0.37	2016-03-20 03:53:19	2016-03-20 04:09:54	995	0.5 ^{+0.8} _{-0.3}
00034135061	57468.01586	0.57	2016-03-21 00:22:35	2016-03-21 00:38:52	30	–
00034135062	57469.62087	0.95	2016-03-22 14:47:12	2016-03-22 15:00:54	822	1.8 ^{+1.1} _{-0.7}
00034135063	57470.08529	0.06	2016-03-23 02:02:35	2016-03-23 02:18:53	28	–
00034135064	57471.88419	0.49	2016-03-24 21:05:35	2016-03-24 21:20:52	321	–
00034135065	57472.87287	0.72	2016-03-25 20:56:39	2016-03-25 21:12:55	33	–
00034135066	57473.71689	0.92	2016-03-26 14:47:45	2016-03-26 19:36:54	802	–
00034135067	57474.24053	0.04	2016-03-27 00:08:48	2016-03-27 11:23:54	822	2.8 ^{+1.0} _{-0.7}
00034135068	57475.72972	0.39	2016-03-28 17:22:41	2016-03-28 17:38:54	973	3.1 ^{+1.2} _{-0.8}

Table C.3: continued.

Sequence	MJD	Phase	Start time (UT)	End time (UT)	Exposure	Flux
00034135069	57476.60286	0.60	2016-03-29 12:53:21	2016-03-29 16:02:53	790	3.1 ^{+1.3} _{-0.9}
00034135070	57477.00666	0.69	2016-03-30 00:03:16	2016-03-30 00:15:54	705	3.7 ^{+1.8} _{-1.2}
00034135071	57478.58739	0.07	2016-03-31 13:56:47	2016-03-31 14:14:53	1086	2.7 ^{+0.9} _{-0.7}
00034135072	57479.78202	0.35	2016-04-01 18:37:19	2016-04-01 18:54:53	1053	2.1 ^{+0.7} _{-0.5}
00034135073	57480.06030	0.41	2016-04-02 01:18:47	2016-04-02 01:34:55	965	2.6 ^{+0.9} _{-0.6}
00034135074	57481.70841	0.80	2016-04-03 16:52:18	2016-04-03 17:07:54	935	2.2 ^{+1.2} _{-0.8}
00034135076	57483.76959	0.29	2016-04-05 18:19:29	2016-04-05 18:36:55	1046	2.9 ^{+1.0} _{-0.7}
00034135077	57484.97279	0.57	2016-04-06 23:12:44	2016-04-06 23:28:54	970	1.9 ^{+0.9} _{-0.6}
00034135078	57485.04257	0.59	2016-04-07 00:53:43	2016-04-07 01:08:53	910	15.6 ^{+4.9} _{-3.7}
00034135079	57486.07752	0.83	2016-04-08 00:59:21	2016-04-08 02:43:53	963	–
00034135080	57487.17528	0.09	2016-04-09 04:05:54	2016-04-09 04:18:54	780	1.4 ^{+0.8} _{-0.5}
00034135081	57488.96274	0.51	2016-04-10 23:02:46	2016-04-10 23:09:55	429	2.0 ^{+2.2} _{-1.0}
00034135082	57489.75842	0.70	2016-04-11 18:11:19	2016-04-11 18:12:55	95	–
00034135083	57490.69493	0.92	2016-04-12 13:25:28	2016-04-12 19:55:55	863	1.7 ^{+1.0} _{-0.6}
00034135084	57491.48572	0.11	2016-04-13 11:31:12	2016-04-13 11:47:55	988	3.6 ^{+1.1} _{-0.8}
00034135085	57492.94566	0.45	2016-04-14 22:33:36	2016-04-14 22:49:54	978	4.0 ^{+1.2} _{-0.9}
00034135086	57493.01501	0.47	2016-04-15 00:13:19	2016-04-15 00:29:54	995	2.8 ^{+0.8} _{-0.6}
00034135087	57494.08169	0.72	2016-04-16 01:50:21	2016-04-16 02:04:54	873	3.1 ^{+1.3} _{-0.9}
00034135088	57495.39796	0.03	2016-04-17 09:26:12	2016-04-17 09:39:54	822	1.2 ^{+0.7} _{-0.4}
00034135089	57496.72762	0.35	2016-04-18 17:18:38	2016-04-18 17:36:53	1096	3.8 ^{+1.0} _{-0.8}
00034135090	57497.92956	0.63	2016-04-19 22:10:13	2016-04-19 22:26:53	998	2.7 ^{+1.0} _{-0.7}
00034135091	57498.39649	0.74	2016-04-20 09:22:59	2016-04-20 09:38:54	930	1.9 ^{+1.0} _{-0.6}
00034135092	57499.13246	0.91	2016-04-21 03:05:36	2016-04-21 03:15:53	617	–
00034135093	57500.52289	0.24	2016-04-22 12:25:02	2016-04-22 12:40:53	950	3.6 ^{+1.3} _{-0.9}
00034135094	57501.25418	0.42	2016-04-23 05:58:07	2016-04-23 06:13:55	948	3.7 ^{+1.2} _{-0.9}
00034135095	57502.05761	0.60	2016-04-24 01:14:00	2016-04-24 01:31:53	1073	4.5 ^{+1.1} _{-0.8}
00034135096	57503.38791	0.92	2016-04-25 09:09:16	2016-04-25 09:27:54	1118	2.8 ^{+1.0} _{-0.8}
00034135097	57504.71843	0.23	2016-04-26 17:06:10	2016-04-26 17:22:53	1003	1.4 ^{+0.5} _{-0.3}
00034135098	57505.31402	0.37	2016-04-27 07:23:12	2016-04-27 07:40:55	1046	2.2 ^{+0.8} _{-0.6}
00034135099	57506.60238	0.68	2016-04-28 13:41:58	2016-04-28 15:12:53	1053	2.1 ^{+1.1} _{-0.7}
00034135100	57507.57783	0.91	2016-04-29 13:43:15	2016-04-29 14:00:53	1058	2.4 ^{+1.1} _{-0.8}
00034135101	57508.57364	0.14	2016-04-30 13:37:10	2016-04-30 13:54:53	1063	–
00034135102	57509.56819	0.38	2016-05-01 13:29:27	2016-05-01 13:46:55	1048	2.4 ^{+1.0} _{-0.7}
00034135103	57510.70142	0.64	2016-05-02 16:42:10	2016-05-02 16:57:53	943	3.8 ^{+1.0} _{-0.8}
00034135104	57511.69894	0.88	2016-05-03 16:39:01	2016-05-03 16:53:54	893	0.3 ^{+0.4} _{-0.1}
00034135105	57512.69870	0.12	2016-05-04 16:37:20	2016-05-04 16:54:53	1053	4.4 ^{+1.4} _{-1.0}
00034135106	57513.21925	0.24	2016-05-05 05:08:31	2016-05-05 05:22:54	863	1.0 ^{+0.7} _{-0.4}
00034135107	57514.28210	0.49	2016-05-06 06:38:33	2016-05-06 06:53:53	918	3.2 ^{+1.0} _{-0.8}
00034135109	57516.60700	0.04	2016-05-08 14:26:16	2016-05-08 14:41:53	938	–
00034135110	57517.74974	0.31	2016-05-09 17:52:18	2016-05-09 18:06:55	878	11.9 ^{+4.0} _{-2.9}
00034135111	57518.66796	0.52	2016-05-10 15:54:50	2016-05-10 16:08:53	842	5.1 ^{+1.5} _{-1.1}
00034135112	57519.60390	0.74	2016-05-11 14:25:18	2016-05-11 19:01:53	517	1.9 ^{+1.4} _{-1.0}
00034135113	57520.66917	1.00	2016-05-12 15:55:18	2016-05-12 16:11:54	995	3.8 ^{+1.4} _{-1.0}
00034135114	57521.07151	0.09	2016-05-13 01:35:03	2016-05-13 01:50:54	950	1.5 ^{+0.7} _{-0.4}
00034135115	57522.71594	0.48	2016-05-14 17:09:48	2016-05-14 17:23:53	35	–
00034135116	57523.31809	0.62	2016-05-15 07:30:11	2016-05-15 07:45:54	943	3.0 ^{+1.0} _{-0.8}
00034135117	57524.31462	0.86	2016-05-16 07:24:11	2016-05-16 07:41:54	1063	–
00034135118	57525.64240	0.17	2016-05-17 15:17:12	2016-05-17 15:32:53	940	2.8 ^{+1.2} _{-0.8}
00034135119	57526.30889	0.33	2016-05-18 07:16:41	2016-05-18 07:32:54	973	1.7 ^{+0.6} _{-0.4}
00034135120	57527.62959	0.64	2016-05-19 15:06:36	2016-05-19 15:22:56	350	–

Table C.3: continued.

Sequence	MJD	Phase	Start time (UT)	End time (UT)	Exposure	Flux
00034135120	57527.63526	0.64	2016-05-19 15:06:40	2016-05-19 15:22:51	213	–
00034135121	57528.08381	0.75	2016-05-20 01:07:28	2016-05-20 02:53:53	1133	2.8 ^{+0.9} _{–0.7}
00034135122	57529.27390	0.03	2016-05-21 02:44:55	2016-05-21 10:23:53	787	1.6 ^{+1.5} _{–0.7}
00034135123	57530.52718	0.32	2016-05-22 11:51:24	2016-05-22 13:26:53	878	1.2 ^{+0.8} _{–0.5}
00034135124	57531.42992	0.54	2016-05-23 10:11:14	2016-05-23 10:26:55	940	2.0 ^{+1.0} _{–0.6}
00034135125	57532.83370	0.87	2016-05-24 19:52:10	2016-05-24 20:08:52	1003	–
00034135126	57533.83165	0.10	2016-05-25 19:50:14	2016-05-25 20:04:54	880	7.7 ^{+1.9} _{–1.6}
00034135127	57534.34778	0.22	2016-05-26 08:12:42	2016-05-26 08:28:53	970	3.5 ^{+1.0} _{–0.8}
00034135128	57535.54997	0.51	2016-05-27 13:04:00	2016-05-27 13:19:55	955	3.1 ^{+1.0} _{–0.7}
00034135129	57536.35117	0.70	2016-05-28 08:25:34	2016-05-28 08:39:54	860	1.7 ^{+1.1} _{–0.7}
00034135130	57537.60277	0.99	2016-05-29 14:20:03	2016-05-29 14:35:54	950	1.5 ^{+0.7} _{–0.4}
00034135131	57538.34686	0.17	2016-05-30 08:11:11	2016-05-30 08:27:54	993	2.8 ^{+0.9} _{–0.7}
00034135132	57539.34113	0.40	2016-05-31 08:03:32	2016-05-31 08:18:55	920	2.3 ^{+1.2} _{–0.7}
00034135133	57540.72807	0.73	2016-06-01 17:19:54	2016-06-01 17:36:55	1020	2.7 ^{+1.0} _{–0.7}
00034135134	57541.46951	0.90	2016-06-02 09:44:16	2016-06-02 12:47:54	567	0.6 ^{+0.3} _{–0.2}
00034135135	57542.59067	0.17	2016-06-03 14:04:12	2016-06-03 14:16:54	762	3.6 ^{+1.2} _{–0.9}
00034135136	57543.38816	0.36	2016-06-04 09:11:59	2016-06-04 09:25:54	835	3.9 ^{+1.6} _{–1.1}
00034135137	57544.46000	0.61	2016-06-05 10:54:52	2016-06-05 11:09:54	903	1.4 ^{+0.7} _{–0.4}
00034135138	57545.91938	0.95	2016-06-06 21:55:54	2016-06-06 22:11:54	960	3.8 ^{+2.5} _{–2.7}
00034135139	57546.71955	0.14	2016-06-07 17:08:24	2016-06-07 17:23:54	930	2.0 ^{+0.8} _{–0.5}
00034135140	57547.74795	0.39	2016-06-08 17:04:11	2016-06-08 18:49:54	847	6.1 ^{+1.6} _{–1.3}
00034135141	57548.90854	0.66	2016-06-09 21:39:42	2016-06-09 21:56:53	1031	3.8 ^{+1.1} _{–0.8}
00034135142	57549.76590	0.86	2016-06-10 18:14:53	2016-06-10 18:30:54	960	–
00034135143	57550.76243	0.10	2016-06-11 18:09:52	2016-06-11 18:25:54	963	2.0 ^{+0.8} _{–0.6}
00034135144	57551.69627	0.32	2016-06-12 16:34:22	2016-06-12 16:50:53	990	7.0 ^{+1.6} _{–1.3}
00034135145	57552.69249	0.55	2016-06-13 16:28:28	2016-06-13 16:45:54	1046	6.1 ^{+1.5} _{–1.2}
00034135146	57553.62090	0.77	2016-06-14 14:45:17	2016-06-14 15:02:55	1058	1.0 ^{+0.8} _{–0.4}
00034135147	57554.55088	0.99	2016-06-15 13:04:37	2016-06-15 13:21:55	1038	4.3 ^{+1.1} _{–0.9}
00034135148	57555.41071	0.19	2016-06-16 08:13:55	2016-06-16 11:28:54	572	2.8 ^{+1.5} _{–1.0}
00034135150	57557.21669	0.62	2016-06-18 05:04:09	2016-06-18 05:19:54	945	2.2 ^{+0.8} _{–0.6}

Table C.4: *Swift* observation log of XTE J1855–026

Sequence/Instr./mode	MJD	Start time (UT) (yyyy-mm-dd hh:mm:ss)	End time (UT) (yyyy-mm-dd hh:mm:ss)	Exposure (s)	Time since trigger (s)
00503434000/BAT/evt	55822.48886	2011-09-18 10:03:35	2011-09-18T13:24:19	1257	–239–11805
00503434000/XRT/WT	55822.49860	2011-09-18 10:32:44	2011-09-18 13:23:13	629	1510–11740
00503434000/XRT/PC	55822.49932	2011-09-18 10:34:42	2011-09-18 13:23:20	1264	1629–11746

Notes. We show: observing sequence/instrument/mode, date (MJD middle), start and end times (UT), exposure time and time since the trigger.

Table C.5: *Swift*/XRT observation log for IGR J17503–2636.

Sequence	MJD	Start time (UT)	End time (UT)	Exposure	N_{H}	Γ	$F_{0.3-10 \text{ keV}}$	Cstat/d.o.f.
00010980001	58576.71546	2019-04-03 17:10:15	2019-04-03 22:17:53	5178	$8.3^{+1.8}_{-1.6}$	$2.8^{+0.9}_{-0.8}$	$0.9^{+0.1}_{-0.1}$	120.2/142
00010980002	58583.49265	2019-04-10 11:49:25	2019-04-10 15:26:52	3372	$5.7^{+1.5}_{-1.2}$	$2.6^{+1.0}_{-0.9}$	$1.0^{+0.2}_{-0.1}$	83.9/116
00010980003	58590.53303	2019-04-17 12:47:33	2019-04-17 20:56:53	4944	$2.0^{+1.4}_{-0.8}$	$-0.4^{+0.9}_{-0.7}$	$0.7^{+0.2}_{-0.1}$	95.2/79
00010980005	58611.77889	2019-05-08 18:41:35	2019-05-08 22:20:52	4012	$5.3^{+0.8}_{-0.7}$	$1.7^{+0.5}_{-0.5}$	$3.4^{+0.3}_{-0.3}$	229.8/278
00010980006	58618.10236	2019-05-15 02:27:23	2019-05-15 15:10:53	4897	$8.4^{+1.2}_{-1.1}$	$1.3^{+0.5}_{-0.5}$	$3.3^{+0.3}_{-0.2}$	216.9/279
00010980007	58643.79713	2019-06-09 19:07:51	2019-06-10 00:06:53	4734	$4.3^{+0.7}_{-0.6}$	$1.5^{+0.5}_{-0.4}$	$2.5^{+0.2}_{-0.2}$	219.1/269
00010807001	58343.82179	2018-08-13 19:43:22	2018-08-13 20:13:11	990	$2.0^{+0.7}_{-0.5}$	$0.1^{+0.5}_{-0.5}$	$14.7^{+1.9}_{-1.6}$	118.2/156
00088805001	58353.19412	2018-08-23 04:39:32	2018-08-23 06:38:52	1858	$8.2^{+2.7}_{-2.2}$	$1.1^{+1.2}_{-1.0}$	$1.9^{+0.4}_{-0.3}$	70.0/82
00048022007	56224.21009	2012-10-24 05:02:31	2012-10-24 05:30:54	1702	$0.5^{+0.4}_{-0.2}$	$1.9^{+1.0}_{-0.8}$	$0.5^{+0.2}_{-0.1}$	44.4/47

Notes. We show: observing sequence, date (MJD of the middle of the observation), start and end times (UT), and XRT exposure time in seconds. We also report the absorption column density N_{H} in units of 10^{23} cm^{-2} , the powerlaw photon index Γ , and the flux in the 0.3–10 keV energy band (not corrected for absorption in units of $10^{-11} \text{ erg cm}^{-2} \text{ s}^{-1}$) as determined from the spectral fit.